ACS NANO

www.acsnano.org

ARTICLE

Live Microscopy of Multicellular Spheroids with the Multimodal Near-Infrared Nanoparticles Reveals Differences in Oxygenation Gradients

Angela C. Debruyne, Irina A. Okkelman, Nina Heymans, Cláudio Pinheiro, An Hendrix, Max Nobis, Sergey M. Borisov,* and Ruslan I. Dmitriev*

Cite This: *ACS Nano* 2024, 18, 12168–12186

Read Online

ACCESS | Metrics & More | Article Recommendations | Supporting Information

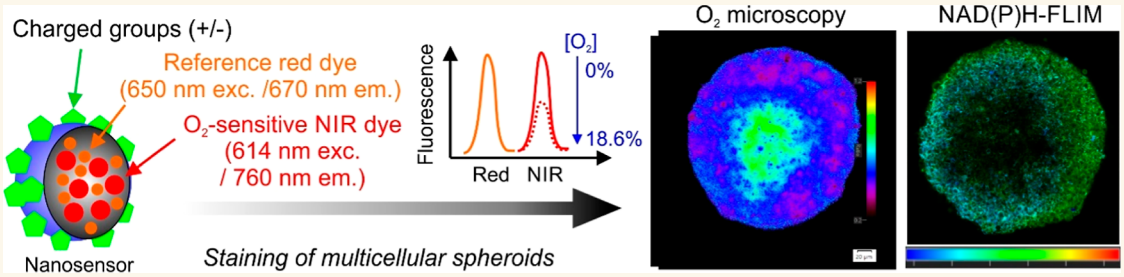

ABSTRACT: **Assessment of hypoxia, nutrients, metabolite gradients, and other hallmarks of the tumor microenvironment within 3D multicellular spheroid and organoid models represents a challenging analytical task. Here, we report red/near-infrared (NIR) emitting cell staining with O_2-sensitive nanoparticles, which enable measurements of spheroid oxygenation on a conventional fluorescence microscope. Nanosensor probes, termed "MMIR" (multimodal infrared), incorporate an NIR O_2-sensitive metalloporphyrin (PtTPTBPF) and deep red aza-BODIPY reference dyes within a biocompatible polymer shell, allowing for oxygen gradient quantification via fluorescence ratio and phosphorescence lifetime readouts. We optimized staining techniques and evaluated the nanosensor probe characteristics and cytotoxicity. Subsequently, we applied nanosensors to the live spheroid models based on HCT116, DPSCs, and SKOV3 cells, at rest, and treated with drugs affecting cell respiration. We found that the growth medium viscosity, spheroid size, and formation method influenced spheroid oxygenation. Some spheroids produced from HCT116 and dental pulp stem cells exhibited "inverted" oxygenation gradients, with higher core oxygen levels than the periphery. This contrasted with the frequently encountered "normal" gradient of hypoxia toward the core caused by diffusion. Further microscopy analysis of spheroids with an "inverted" gradient demonstrated metabolic stratification of cells within spheroids: thus, autofluorescence FLIM of NAD(P)H indicated the formation of a glycolytic core and localization of OxPhos-active cells at the periphery. Collectively, we demonstrate a strong potential of NIR-emitting ratiometric nanosensors for advanced microscopy studies targeting live and quantitative real-time monitoring of cell metabolism and hypoxia in complex 3D tissue models.**

KEYWORDS: *cancer, hypoxia, fluorescence microscopy, FLIM, multicellular spheroids, nanoparticles, oxygenation*

Oxygen is a key metabolite for cell metabolism and energy production in the form of adenosine triphosphate (ATP), via oxidative phosphorylation. Under physiological normoxia, the O_2 supply and consumption are balanced, while in hypoxia (or oxygen-deprived conditions, compared to physiological tissue level), the O_2 concentration is below the norm. Different tissues often show different oxygen requirements depending on their function, metabolite consumption, and vascular oxygen supply, typically ranging from 2 to 9% O_2 (14–65 mmHg).[1]

Received: December 12, 2023
Revised: April 6, 2024
Accepted: April 15, 2024
Published: April 30, 2024

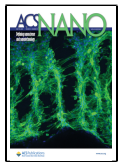

https://doi.org/10.1021/acsnano.3c12539
ACS Nano 2024, 18, 12168–12186

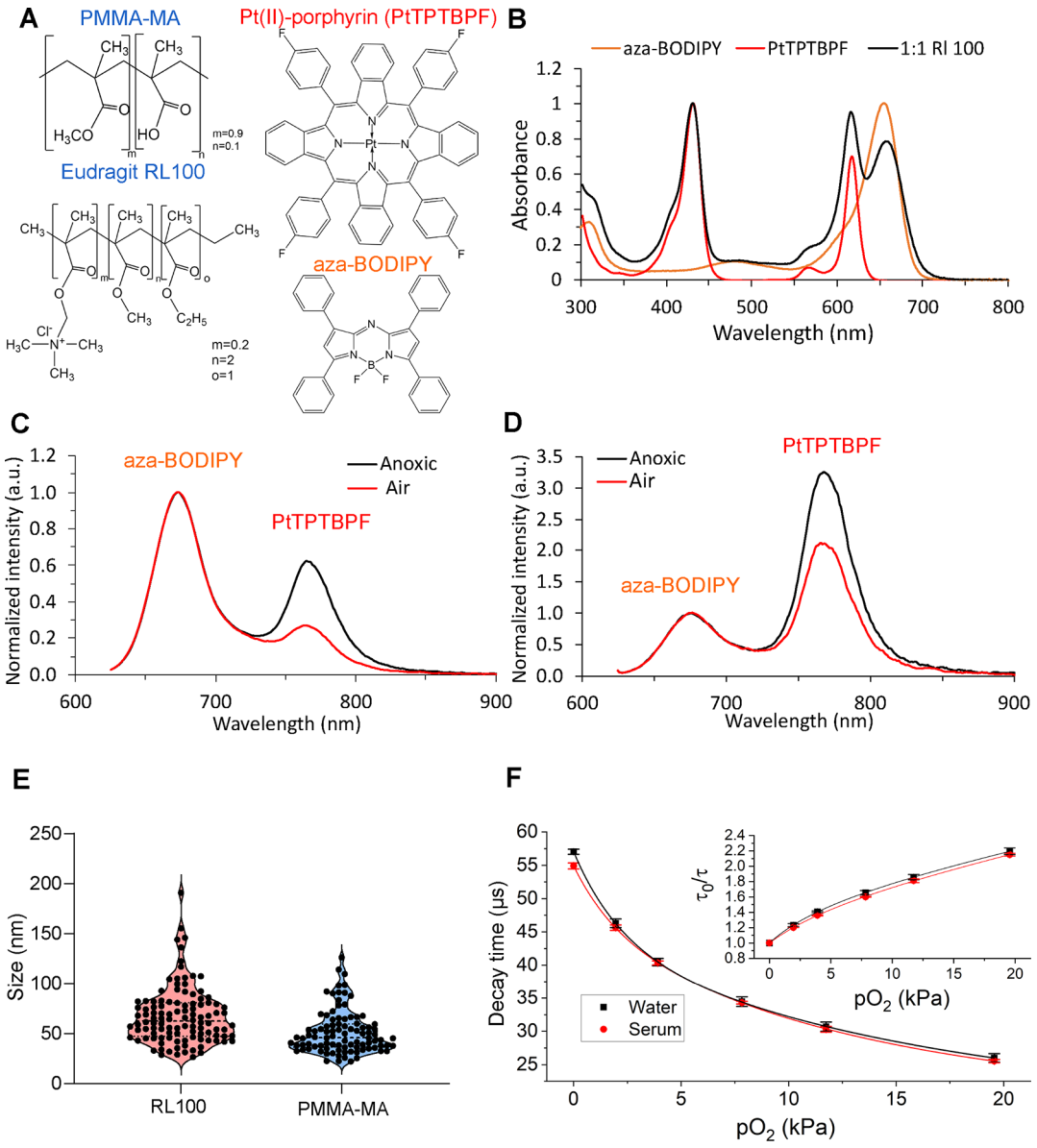

Figure 1. Chemical and spectral characterization of MMIR O_2 probes. (A) Chemical structures of the reference dye (aza-BODIPY) and O_2-sensitive (PtTPTBPF) coprecipitated in either PMMA-MA or Eudragit RL100 NPs. (B) Absorption spectra of the resulting MMIR probes (1:1 dye ratio) as well as the absorption spectra of both dyes in toluene solution. (C) Emission spectra of the MMIR probe (1:1 ratio of PtTPTBPF to aza-BODIPY) in anoxic and air-saturated water (λ_{exc} 615 nm). (D) Emission spectra of the MMIR− probe (1:1 ratio of PtTPTBPF to aza-BODIPY) in anoxic and air-saturated water (λ_{exc} 615 nm). (E) Size distribution of the RL100 (N = 230) and PMMA-MA (N = 190) NPs measured using a transmission electron microscope. (F) O_2 response and Stern−Volmer relationship (inset) for the phosphorescence lifetime of MMIR1, (23 °C) in water (black) and 10% serum (red). The data represent an average for three different batches of the material.

Hypoxia results in diminished mitochondrial activity, overproduction of reactive oxygen and nitrogen (RNS)[2] species, activation of hypoxia-inducible factor (HIF)-dependent pathways, and ultimately cell death.[3,4] Therefore, the heterogeneity of cell and tissue oxygenation plays an important role in tissue development and homeostasis. Hypoxia is associated with ischemia,[5,6] cancer,[7] cardiovascular disorders,[8] inflammatory,[9,10] and infectious diseases.[11−13] In solid tumors, uncontrolled cell proliferation and abnormal vascularisation lead to hypoxia,[14] resulting in poor prognosis, increased cancer cell survival, metabolic switch from oxidative phosphorylation toward aerobic glycolysis,[15] increased cell migration,[16] and resistance to therapy.[17] 3D tumor spheroids have been widely used to study oxygenation gradients and hypoxia in vitro, as promising models to bridge the gap between monolayer cultures and intravital experiments, mimicking organ-specific tissue architecture and microenvironment.[18−21] Typically, tumor spheroids larger than 300−500 μm in diameter are expected to consist of three concentric layers,[22−24] representing the proliferating, quiescent, and necrotic core, due to nutrients and oxygen diffusion limits concomitant with accumulation of waste products, lactate, and decreasing pH.[25,26]

Traditional methods for (intra)cellular oxygen measurements and oxygen consumption rates (OCR) in such 3D models as spheroids, neurospheres, organoids, and (micro)-

https://doi.org/10.1021/acsnano.3c12539
ACS Nano 2024, 18, 12168−12186

scaffold-grown structures include microelectrodes,[27] redox-sensitive nitroimidazole derivatives,[28] indirect staining with antibodies and hypoxia markers (such as HIF-1α),[29] genetically encoded fluorescent reporters,[30,31] organ-on-a-chip devices coupled with solid-state sensors,[32,33] optical-based multiwell plate systems,[34,35] and optical methods using fluorescent[36−38] and phosphorescent[39−44] probes. Optical sensing of molecular oxygen (O_2) has gained significant interest, as it allows for live monitoring of cell metabolism, OCR, and oxygen gradient in a direct, noninvasive, non-chemical, and highly sensitive manner with broad possibilities for multiplexing.[45] O_2 indicators are designed based on the phosphorescence quenching phenomenon of the macrocyclic metal complexes, such as Pt(II),[46,47] Pd(II)[48] metalloporphyrins, and Ru(II) polypyridyl complexes,[49] where O_2 interacts with molecules in the triplet-excited states causing a non-emissive deactivation of the phosphor, resulting in a reduction in luminescence.[50] Thus, higher O_2 levels lead to lower phosphorescence intensity and shorter decay times (lifetimes), while lower O_2 levels lead to higher phosphorescence intensities and longer lifetimes.[51]

Phosphorescent probes are commonly designed to be shielded from undesirable microenvironmental effects by adding a physical barrier, via chemical modification with protective chemical groups,[52−54] or being encapsulated into biocompatible and oxygen-permeable nanoparticles (NPs).[45] Chemical modification can help improve cell penetration and biocompatibility, while polymer encapsulation fine-tunes the quenching sensitivity and protects indicators from local environmental influences (e.g., low pH) and interactions with biological components (e.g., albumin).[55] MitoImage-NanO2 was one of the first-generation NP nanosensors, containing the hydrophobic phosphorescent Pt(II)-tetrakis-(pentafluorophenyl)porphyrin dye (PtPFPP) in the cationic RL-100 polymer, allowing for intracellular O_2 measurement in phosphorescence lifetime imaging microscopy (PLIM) and time-resolved fluorescence plate reader-based measurements of 2D and 3D cell cultures.[56] However, the microscopy setup, the intensity of the excitation light, excitation time, scattering, and sensitivity of the photodetector can influence the phosphorescence intensity of the O_2 indicators. Ratiometric analysis with the help of O_2-sensitive and added insensitive indicators can reduce these effects through the use of internal O_2 calibration,[46] such as with MitoImage MM2 probe,[47] conjugated polymer NPs,[43,57] ratiometric Förster resonance energy transfer (FRET) NPs,[58,59] polymer dots,[60] and negatively charged poly(methyl methacrylate-*co*-methacrylic acid) (PMMA-MA) NPs.[61]

Surprisingly, there has been little attention to the use of deep-red and near-infrared (NIR) dyes in O_2 imaging so far.[62−65] Using such structures with long-wave excitation and emission would provide decreased phototoxicity, ensure better filtering of the autofluorescence,[66] and provide deeper light penetration across the volume of multicellular spheroids. While some progress has been achieved with the dye- and fluorescent protein-based structures, their use in ratiometric measurements in imaging of 3D microtissues is still rare.[41,67−70] Here, we demonstrate the red/NIR-emitting NP probes, which provide nontoxic, stable, and cell line-dependent staining and can be used for long-term monitoring of rapid changes in oxygenation in multicellular spheroids. We also validate the detection of observed gradients with the label-free two-photon FLIM microscopy of NAD(P)H. Collectively, the presented approach should help to standardize studies probing hypoxia in 3D tissue models.

RESULTS AND DISCUSSION

Design and Spectral Characterization of the Multimodal Infrared (MMIR) Probes. To ensure more efficient O_2-sensing with the help of far-red and NIR dyes, we designed MMIR sensor probes by the nanoprecipitation technique,[71] in which the O_2-sensitive phosphorescent reporter dye, PtTPTBPF[72,73] (exc. 620 nm, em. 760 nm), and the reference O_2-insensitive fluorophore aza-BODIPY[74] (exc. 650 nm, em. 675 nm) are impregnated in the NP-forming cationic polymer RL-100 (Eudragit) (Figure 1A,B). The dyes were selected according to the following criteria: (i) hydrophobicity to ensure no leaching and stability in the NPs; (ii) efficient excitation in the red part of the spectrum for better compatibility with biological probes; (iii) significantly different position of the emission maxima for ratiometric read-out; and (iv) absence of spectral overlap between the emission of the oxygen indicator and the absorption of the reference dye and between the emission of the reference dye and the absorption of the oxygen indicator in order to avoid FRET. Figure 1B−D shows that these conditions are fulfilled for the selected pair of dyes. It should be noted that PtTPTBPF is also commercially available, and the aza-BODIPY dye can be prepared with moderate synthetic effort.[74] As can be seen from Figures S3 and S4, the particles can be prepared in a reproducible manner. Not surprisingly, the emission ratio is significantly influenced by the ratio of both emitters so that resulting spectral properties can be affected by possible errors (during dye weighing and pipetting of stock solutions), as was observed for batch 1 of MMIR beads. To minimize such fluctuations, it is therefore advisable to produce larger batches of the NPs (i.e., $\gg$50 mg, the amount used in this work). UV−vis spectroscopy appears to give a simple way to screen for potential flaws in particle preparation (Figure S3). Initial screening was performed with different dye ratios (1:1, 1:0.5, and 0.5:1) to select the most optimal material with respect to the available microscope detector. Although all further experiments were performed with a 1:1 ratio of the dyes (both 1 wt % % with respect to the polymer), it is easily possible to adjust the ratio for other equipment if necessary. The particles were found to be suitable for storage (4 °C) over a prolonged period (months and even years) without noticeable aggregation or increase in turbidity (Figure S5).

Previous work[61] showed that the anionic PMMA-MA NP PA2 showed better staining of multiple neural cell lines and 3D tissue models and had fewer precipitation issues compared to the cationic NPs.[40] Therefore, we also produced such a probe termed "MMIR−", containing 1 wt % aza-BODIPY and 1 wt % PtTPTBPF (Figure 1A). This material also showed ratiometric oxygen sensing capability (Figure 1D), but the sensitivity to oxygen was much lower than in the case of the MMIR1 probe, which is explained by higher permeability of the polymer matrix for the latter. Despite the identical ratio of both dyes in MMIR1 and MMIR− materials (Figure S3), the emission spectra of the latter indicate a significantly stronger contribution from the oxygen indicator compared to the reference dye (Figure S4). Excitation of both dispersions used in the same concentration and showing identical absorption at the excitation wavelength revealed comparable emission intensities for PtTPTBPF in MMIR1 and MMIR− (Figure S6). However, the fluorescence of aza-BODIPY appeared to be

https://doi.org/10.1021/acsnano.3c12539
ACS Nano 2024, 18, 12168−12186

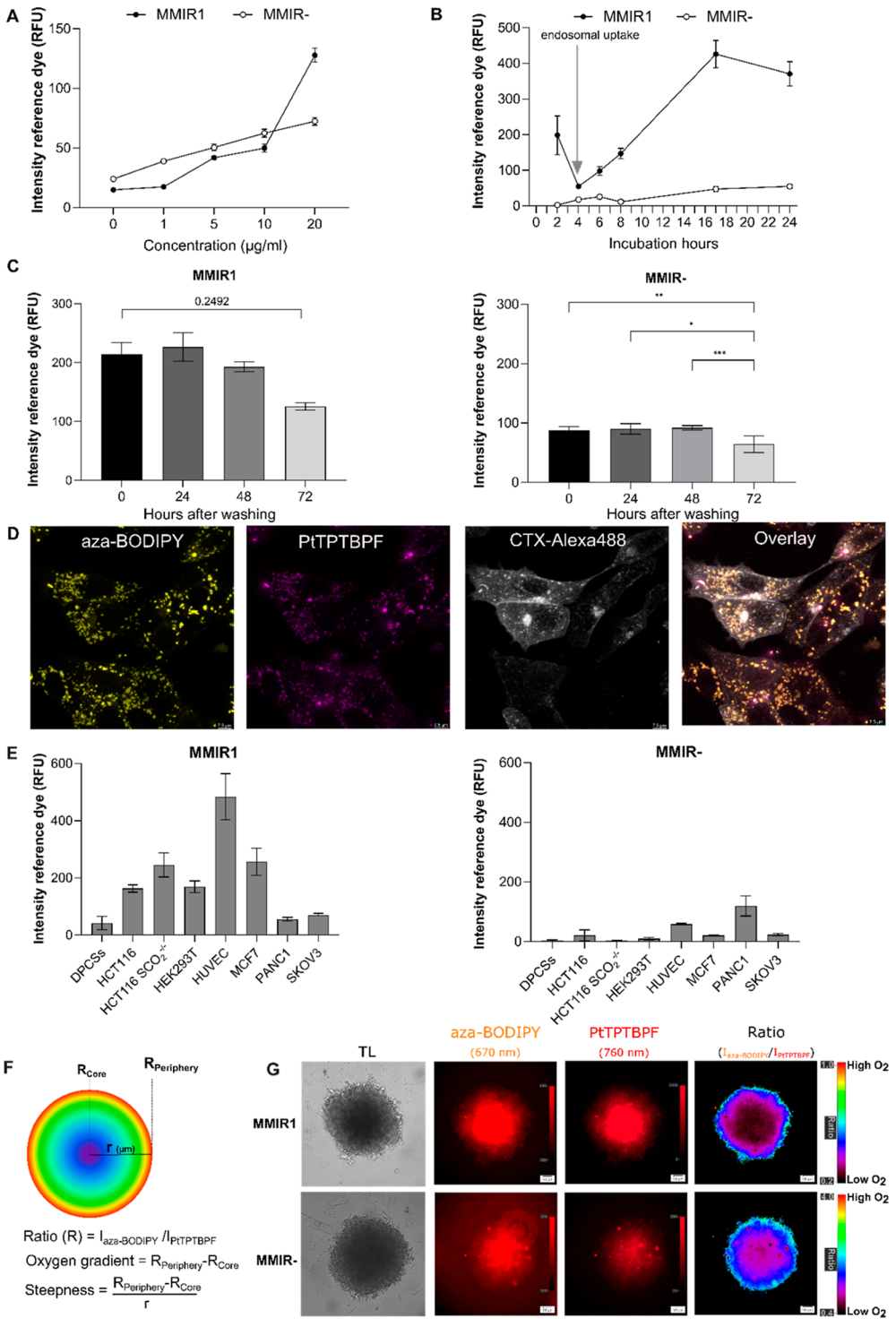

Figure 2. Cell staining and localization of MMIRs in live cells. (A) Concentration dependence of intracellular uptake of MMIR probes. HCT116 cells were incubated with NPs (0−20 μg/mL, 18 h), washed, and quantified on a fluorescence microscope. Data shows the average of 3 repeats (no background subtraction) ±SEM. (B) Time-dependent staining of HCT116 cells with MMIR NPs. Cells were incubated MMIR (0−24 h, 5 μg/mL for MMIR1 or 20 μg/mL for MMIR−). Data shows the average of 5 repeats (with background subtraction) ±SEM. (C) Retention of fluorescent signals (reference dye) of MMIR1 (5 μg/mL, 17 h) and MMIR− (20 μg/mL, 17 h) in HCT116 cells after staining. The data shown are an average of 4 repeats (with background subtraction) ±SEM *: P = 0.0158, **: P = 0.0091, ***: P = 0.0002. (D) Intracellular localization of MMIR1 after overnight incubation with HCT116 cells (5 μg/mL, 17 h) shows endo- and lysosomal localization. Cells were costained with Cholera Toxin-Alexa Fluor 488 (2 μM, 1 h) and imaged using confocal microscopy. Scale bar is 7.5 μm. (E) Cell line-dependent uptake of the MMIR1 and MMIR−probes (5 μg/mL, 17 h), based on fluorescence microscopy experiments. Data show the average of 3 replicates (with background subtraction) ±SEM. (F) Quantitative formulas for statistical analysis. R = Ratio, I = intensity, r = radius. (G) Ratiometric imaging of the oxygen gradient using MMIR1 and MMIR− probes in live SKOV3 cell spheroids with the shown transmission light, sensitive, and reference dye intensity images. Scale bar is 100 μm.

https://doi.org/10.1021/acsnano.3c12539
ACS Nano 2024, 18, 12168−12186

significantly quenched (~10 fold) in MMIR− compared to MMIR1. Measurement of fluorescence decay times revealed a similar degree of quenching (Figure S7) with decay times of 4.3 and ~0.5 ns in MMIR1 and MMIR−, respectively. This may be due to poor compatibility of the reference dye with the PMMA-MA matrix resulting in aggregation of the fluorophore since the decay time for the NPs that contained only the aza-BODIPY dye was also short (~1.6 ns). In contrast to the reference dye, PtTPTBPF was much more compatible with the PMMA-MA matrix. In fact, the measurement of phosphorescence decay times of PtTPTBPF in MMIR1 and MMIR− materials (Figures S8 and S9) did not show such a drastic quenching (decay times in deoxygenated conditions of 57 and 39 μs, respectively).

The morphology and size of both MMIR NP types were analyzed by TEM and dynamic light scattering (NP tracking analysis, NTA). Interestingly, NTA revealed (Figure S10A) that PMMA-MA displayed high reproducibility of production and size distribution of ~64 nm, while RL100-based NPs did not efficiently scatter the light and their size was seemingly in the range of <60 nm, comparable with previously reported size measurements for MM2 (70 nm) and PA2 (95 nm) probes.[61,74] TEM showed similar results (~68 nm for RL-100 and ~52 nm for PMMA-MA) but with less regular shapes, which can be explained by the aggregation of these polymers when present in a dried form (Figures 1E and S10B). Thus, PMMA-MA in the dried form (TEM) displayed a smaller size, which could be explained by the differences in the size of the hydration shell and scattering efficiency.

Next to the possibility of fluorescence intensity-based ratiometric analysis using common widefield and confocal fluorescence microscopy, the NPs should also display O_2-sensitive phosphorescence lifetime changes measurable by PLIM. We performed calibration of MMIR1 in water and 10% serum (mimicking cell environment) and found a minor effect of serum, slightly reducing the luminescence decay times. This can be explained by the fact that some population of the dye is still exposed to the "external" microenvironment and is not fully protected, due to the nature of the nanoprecipitation technique. Nevertheless, the effect was minor (an average of 4%) and we concluded that NPs provide good protection against interferences from serum and other biological components (Figure 1F). These measurements also indicated high reproducibility of the oxygen sensing properties for different batches of the material, even if the ratio of both emitters is slightly varied. For the subsequent experiments, we decided to focus on ratiometric semiquantitative detection, as the most widely available and affordable microscopy readout.

Cell Staining, Localization, and Effects on Cell Viability of MMIR Probes. First, a selection of the produced NPs was made based on their staining efficiency after overnight staining (17 h) with a "standard" concentration for NPs (5 μg/mL) on adherent cell monolayer cultures, including human colon cancer cells (HCT116), human dental pulp stem cells (hDSPCs), and human umbilical vein endothelial cells (HUVECs) (Figure S11). Positively charged particles displayed an overall higher fluorescence intensity compared with the negatively charged ones. As expected, MMIR− showed fewer probe aggregation when in contact with cells, compared to the cationic MMIR1 (0.5:1 and 1:0.5 ratios) (Figures S11A,B). Subsequently, we selected MMIR− and MMIR1 for the following tests on the effects on cell staining, localization, cell viability, and experiments with 3D cultures.

We studied NP concentration-dependent cell staining using overnight incubation with a range of concentrations (0−20 μg/mL) (Figure 2A). This helped us to find 5 μg/mL as a sufficient staining concentration for MMIR1 and 20 μg/mL for MMIR−. Next, we looked at the kinetics of cell staining and found that NPs showed intracellular uptake after 4 h of incubation, reaching maximal signals after 17 h for MMIR1 (Figure 2B). Longer incubation led to noticeable precipitation outside the cells. MMIR− showed a steady increase in intracellular signal even after 24 h.

To investigate how long NPs could remain inside the cells, we performed a "leakage" experiment over 72 h (Figure 2C). The MMIR1 remained in the cells with a nonsignificant reduction of reference dye intensity for up to 72 h (P = 0.2492), while the MMIR− probe had a significant reduction of signals after 72 h (P = 0.0091). These differences can be explained by probe dilution upon cell division and different cell entry mechanisms, dependent on the type of NPs. With spheroid cultures, we found that keeping MMIR1 in the growth media resulted in long-term retention for up to 26 days (Figure S12).

Cells take up most commonly available O_2 sensing NPs through the mixed endocytosis mechanisms,[56,75] leading to predominantly endo- and lysosomal localization. This was confirmed with our MMIR probes by incubating live HCT116 cells overnight with MMIR1 (5 μg/mL) and costained with green organelle-specific marker dyes (Figures 2D and S13). The mixed endocytosis mechanism was further confirmed by the cell-line-dependent staining efficiency for both NP types (Figure 2E). MMIR1 efficiently stained most cancer and noncancer cell lines, while for MMIR−, more cell-specific behavior was noted (Figure S14).

Considering the rate and mechanism of cell entry for MMIR probes, we could stain 3D multicellular spheroid models by adding NPs during spheroid formation or forming spheroids from already prestained cells (Figure S15). This method ensures improved distribution of NPs through the volume of spheroids of different sizes and different cell types, including HCT116, DPSC, MDA-MB-231, and SKOV3. Ratiometric analysis ensures the visualization of the oxygen gradients in the spheroids, through the normalization of the fluorescence intensity of the reference by the sensitive dye signal. Previously,[63] we introduced the parameters "oxygen gradient" ($R_{periphery} - R_{core}$) and "steepness" (Δratio/spheroid radius), hereby making quantitative measurements possible (Figure 2F). Thus, ovarian adenocarcinoma SKOV3 cells internalized both MMIR NP types with a similar efficiency (Figure 2E), and SKOV3 spheroids displayed comparable oxygenation gradients (Figure 2G).

Potential cytotoxic effects of MMIR NPs were investigated with both 2D monolayer and 3D spheroid cultures. We looked first at the membrane integrity assay with Sytox Green dye and saw no statistically significant effects on cell viability (Figure S16A). Furthermore, we measured total cell ATP levels and saw no effect for the concentration range of MMIR1 up to 50 μg/mL for HCT116 cells (Figure S16B). This was also confirmed by the less direct MTS viability assay method (Figure S17). MMIR1 also did not influence cellular ATP levels upon activation of mitochondria with uncoupler FCCP and inhibitor Oligomycin, confirming no effect on oxidative phosphorylation (Figure S16C). To confirm the low potential cytotoxicity of the MMIR1 to the cells, we tested its effect at the highest staining concentration (50 μg/mL) on the broader

https://doi.org/10.1021/acsnano.3c12539
ACS Nano 2024, 18, 12168−12186

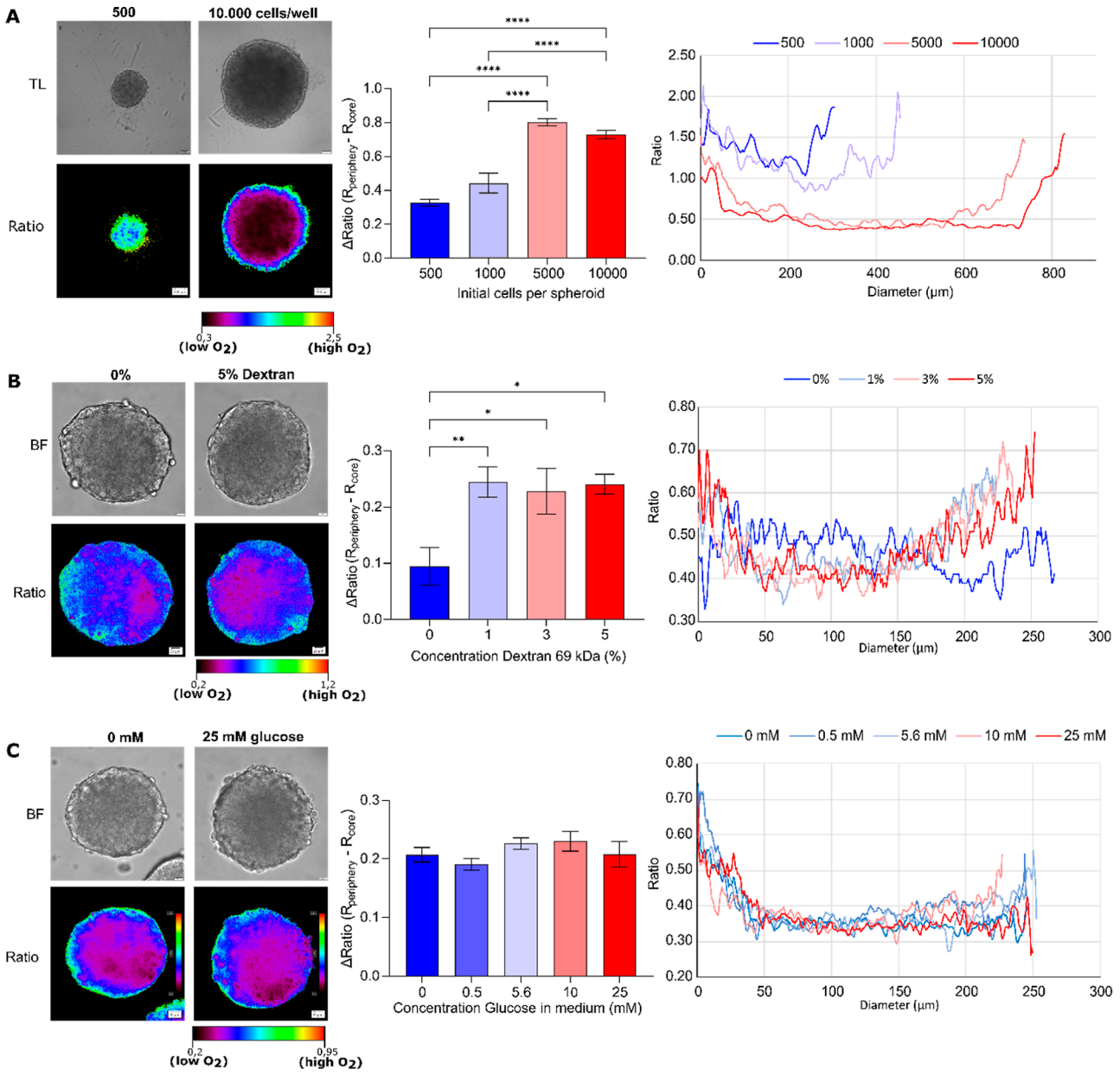

Figure 3. Oxygenation gradients are influenced by size, extracellular viscosity, and glucose concentration. (A) Size-dependent oxygenation of live HCT116 spheroids. HCT116 spheroids formed on a Lipidure-coated plate from 500, 1000, 5000, and 10,000 cells per well (5 days). Results show the average ± standard error of 6 spheroids. Scale bar is 100 μm. (B) Increased cell media viscosity results in the formation of a more hypoxic core. HCT116 spheroids formed using the agarose micromold method were adapted to imaging media containing 0−5 w/w % dextran (0.77−2.25 cP) for 4 h before imaging. Scale bar is 20 μm. Results show the average ± standard error of 9 spheroids. (C) Effect of glucose concentration on oxygenation of live HCT116 spheroids. Spheroids were formed using the agarose micromold method and adapted to imaging media containing 0−25 mM glucose. Scale bar is 20 μm. Results show the average ± standard error of 9−14 spheroids.

panel of cell lines, which we used for cell staining experiments (Figure S16D): no statistically significant effect on the cell function was observed. For HCT116 cells, we extended our tests to 3D cell culture and looked at the effects of staining with MMIR1 on resting ATP in spheroids using the CellTiter-Glo 3D viability assay (Figure S16E). Finally, we also looked at the effects on the distribution of fluorescence lifetimes of endogenous NAD(P)H in MMIR1-stained spheroids via two-photon FLIM: no effects on cellular redox were observed (Figure S18).

Evaluation of MMIR1 NPs in Monitoring Oxygenation in Multicellular Spheroids. To confirm the photostability of MMIR1 fluorescent signals in stained spheroids, we performed repeated illumination (10 cycles) on a conventional LED-based fluorescence microscope: we observed less than a 5% drop in initial intensity ratio, in agreement with the high photostability reported previously for other nanosensors,[56,75] compared to reference tetramethylrhodamine methyl ester (TMRM, $P < 0.001$) (Figure S19A). Thus, both MMIR probes allow for a dynamic real-time study of rapid respiratory responses to mitochondrial uncouplers, activators, and inhibitors of the electron-transport chain. In HCT116 spheroids, FCCP only displayed a mild uncoupling effect at the spheroid core within 2 min of the drug addition. However, a slight increase in the ratio was observed at the spheroid periphery. This agrees with previously reported metabolic

https://doi.org/10.1021/acsnano.3c12539
ACS Nano 2024, 18, 12168−12186

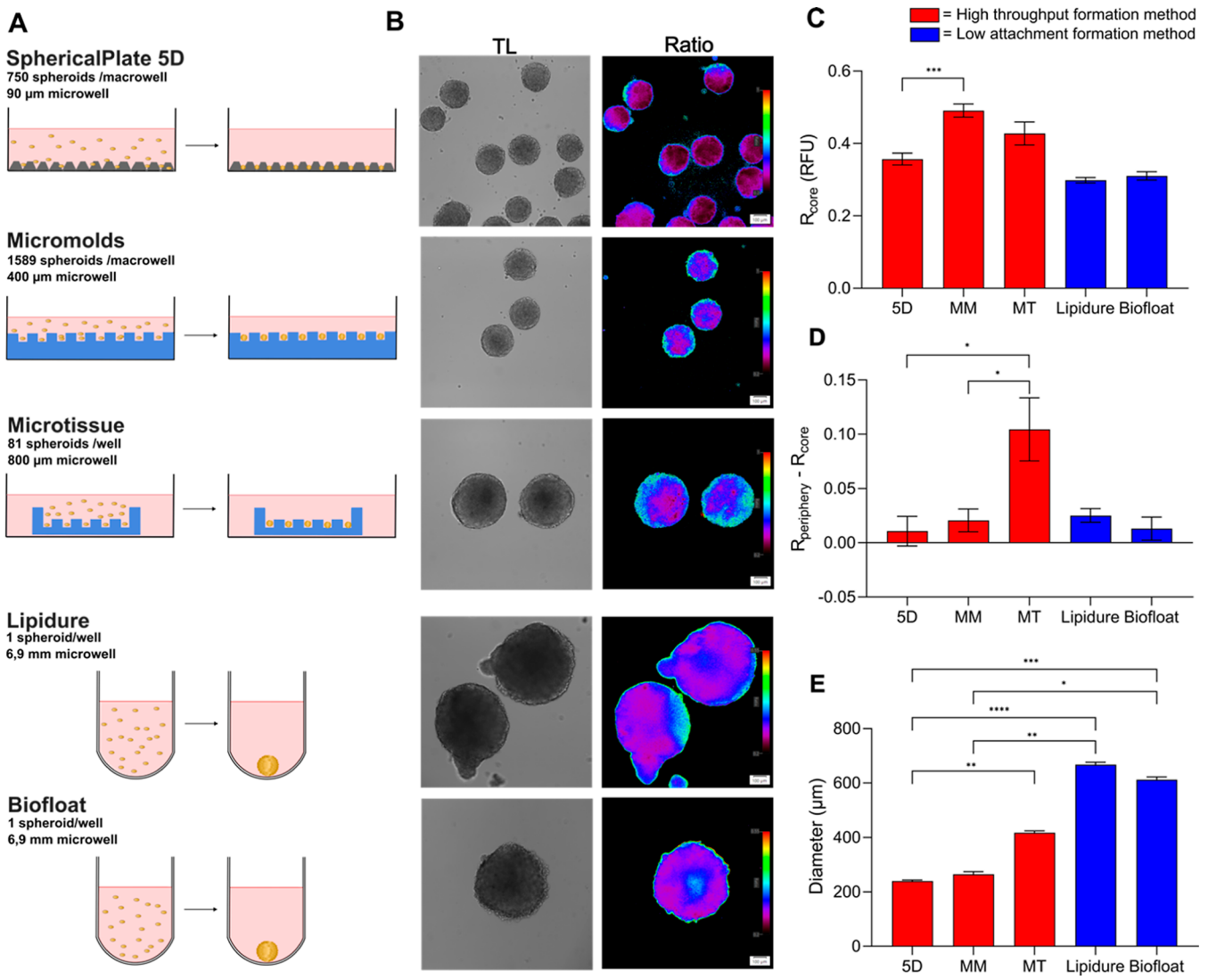

Figure 4. Spheroid formation methods affect morphology, size, viability, and oxygenation. (A) High-throughput methods such as the self-produced micromolds and the microtissue molds use stamps to make multiple microwells in agarose (blue), while the SphericalPlate 5D has integrated patented microwell in the plate. Low-attachment plates such as Lipidure (Amsbio) and Biofloat (Sarstedt) use a nonadherent coating inhibiting cell−surface adhesion and promoting cell self-aggregation. (B) Oxygenation in HCT116 spheroids (initial seeding amount of 500 cells, 20 μg/mL, MMIR1, 6 days) produced by different methods showed more oxygenated spheroids with the microtissue and self-made micromolds than the 5D sphericalplate. (C) MMIR1 ratio measurements at the core. (D) Oxygenation gradients. (E) Spheroid size. Results show the average ± standard error of 6−16 spheroids. 5D = sphericalplate 5D, MM = micromold method, MT = microtissue method.

features of spheroids, which require at least 10 min to display a clear uncoupling effect.[61−63] Rotenone strongly inhibited mitochondrial respiration causing spheroids reoxygenation, leading to an increased ratio % at both spheroid's periphery and core within ∼30 s after stimulation (Figure S19B).

Additionally, responses to O_2 changes were demonstrated in oxygenated (respiratory inhibition by antimycin A and rotenone) and deoxygenated HCT116 spheroids. The ratiometric intensity changes at the periphery were significant ($P < 0.0001$) (Figure S19C). This illustrates the applicability of the ratiometric readout with MMIR probes for the quantitative monitoring of rapid changes in oxygenation in spheroids.

Factors Affecting the Shape of O_2 Gradients in Spheroids. The common mechanism of spheroid formation is based on self-assembly in a nonadherent environment, leading to compactization via *E*-cadherin.[76] Multiple techniques such as micropatterned surfaces, "hanging drop", spinner flasks, use of nonadhesive surfaces, or laser-based 3D bioprinting can produce spheroids of different sizes.[77,78] Even though 3D models gain significant interest compared to 2D cultures, their reproducibility and high variability remain a problem.[40,44,79] Such factors as the nutrient composition of culture media,[79−81] spheroid formation method,[82] and the viscosity of the extracellular fluid[83,84] can contribute to changes in cell viability, differentiation capacity, and response to (bio)chemical signals and thus result in heterogeneity of the grown spheroids and organoids.[85−87]

Multicellular tumor spheroids are considered to be a "simple" model, developing "classical" size-dependent diffusion gradients of nutrients, ATP, waste, and molecular oxygen (O_2), with three concentric structures representing proliferating, quiescent, and necrotic zones.[22−24] In the necrotic core, limited O_2 diffusion creates a hypoxic or anoxic region, which

https://doi.org/10.1021/acsnano.3c12539
ACS Nano 2024, 18, 12168−12186

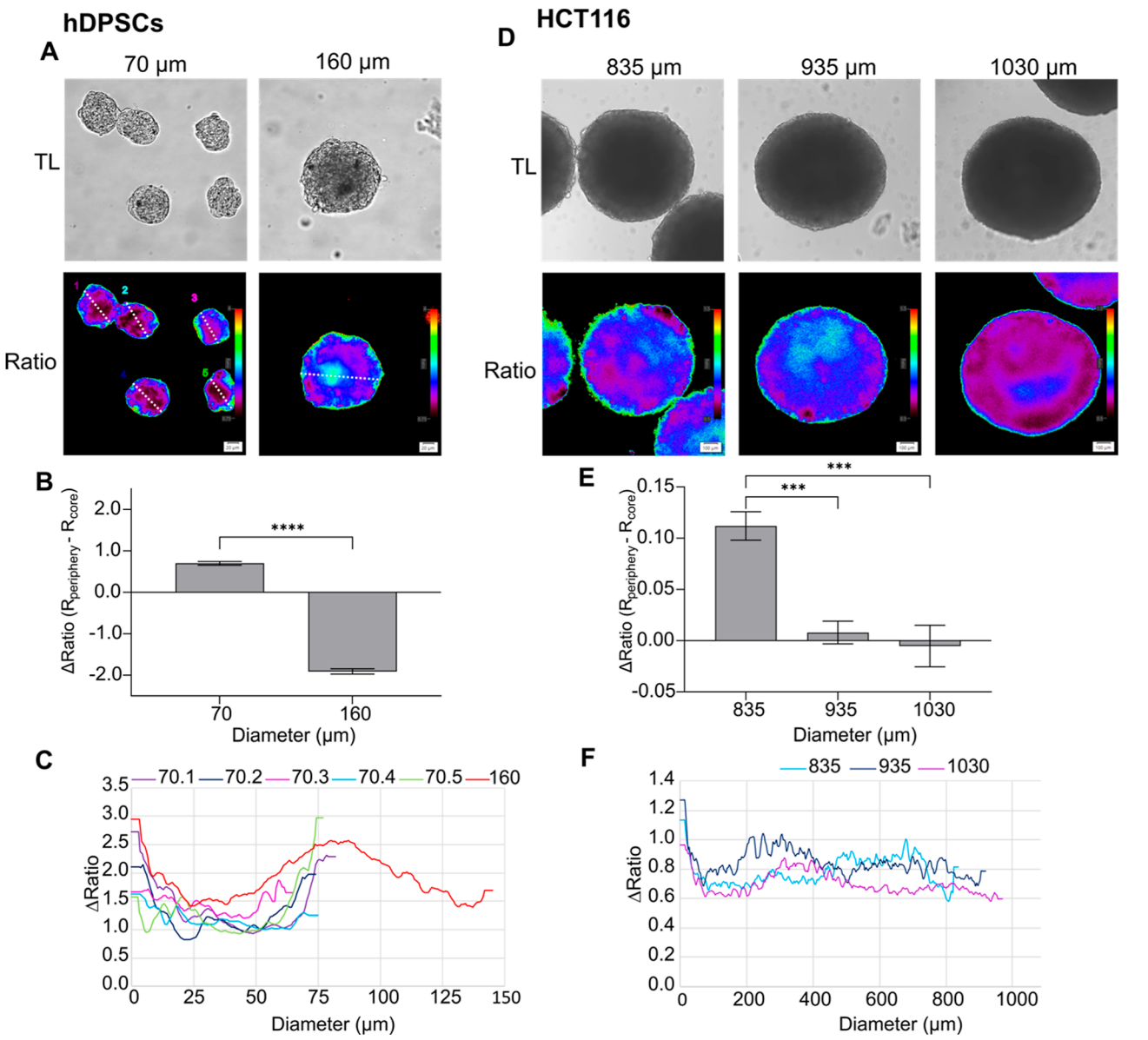

Figure 5. Inverted oxygen gradient in nontumor and tumor spheroids. (A) hDPSCs spheroids formed using agarose micromolds in 2 sizes (70 and 160 μm) for 8 days by respectively seeding 3×10^5 and 1.3×10^6 cells per macromold. Scale bar is 20 μm. (B) Oxygenation gradient is measured by subtraction of the R_{core} from $R_{Periphery}$. Results show the average ± standard error of 30−33 spheroids. ****: $P < 0.0001$. (C) Ratiometric line profiles show increased oxygenation at the core in bigger spheroids. (D) HCT116 spheroids (P. Hwang, NIH cell line) formed for 7 days on Lipidure-coated plate (Amsbio) by initially seeding 1000, 10,000, and 20,000 cells per spheroid, resulting in respectively 835, 935, and 1030 μm diameter. Scale bar is 100 μm. (E) Oxygenation gradient is measured by subtraction of the R_{core} from $R_{Periphery}$. Results show the average ± standard error of 8−10 spheroids. ***: $P < 0.005$. (F) Ratiometric line profiles show an increased oxygenation at spheroids >835 μm.

can be visualized by using our O_2 probe. Thus, live HCT116 spheroids showed size-dependent changes in their oxygenation (Figures 3A and S20A) at the core and periphery (Figure S20B,C). However, the oxygenation steepness, or changes in oxygen gradient per μm, were not significantly size-dependent (Figure S20D).

Extracellular fluid viscosity has been recently shown to increase the motility of various 2D breast cancer cell lines (e.g., MDA-MB-231) and cell dissemination in 3D tumor spheroids.[83,84] However, increased viscosity should also lower the oxygen delivery and result in a more hypoxic environment, which was not studied by Bera et al.[84] To test this, we exposed live HCT116 spheroids to the growth media of higher viscosity, by supplementing with 0−5 w/w % dextran (0.77−2.5 cP, 4 h) (Figure S21). We found that spheroids incubated under higher viscosity compared to growth media (0.77 cP) showed a significant increase in oxygenation gradient (Figure 3B), produced a more hypoxic core (Figure S21C), and significantly increased steepness of oxygenation (core to periphery) (Figure S21D). Thus, an increased extracellular viscosity can also contribute to the "hypoxic cell priming" and affect the metastatic cell dissemination.[88]

We also reasoned that the glucose concentration in the medium could influence oxygenation in spheroids, similar to our previous findings with small intestinal organoids[89] and indirect evidence from the literature.[79] Thus, we looked at the

https://doi.org/10.1021/acsnano.3c12539
ACS Nano 2024, 18, 12168−12186

effect of acute change of the medium glucose content (0−25 mM, 4 h) on the oxygenation of the HCT116 spheroids (Figure S22). Interestingly, while there were some changes in oxygenation and steepness (Figure S22D), they were not statistically significant (Figure 3C). This means that short-term changes (2−4 h) in the growth medium may not significantly affect spheroid oxygenation (and potentially cell metabolism and viability), in contrast to longer-term exposure times (5−7 days) affecting cell death as seen by Baye and co-workers.[90]

The spheroid formation method can considerably influence spheroids' variability, size, and shape, resulting in cell density, and drug sensitivity.[62,79,82,91] Therefore, we investigated how the different high throughput (SphericalPlate 5D, self-made micromolds, and Microtissue molds) and the "medium throughput" low attachment (Biofloat and Lipidure-coated 96-well plates) methods affect the oxygenation, morphology, and viability of HCT116 spheroids (Figure 4).

The chosen high throughput methods use either integrated grids or microwells in agarose to produce multiple spheroids, while a nonadhesive coating is used in the low-attachment plates hereby stimulating self-assembly (Figure 4A). Surprisingly, spheroids formed on low attachment plates were significantly larger, with 667.5 ± 22.65 μm (Lipidure) and 612 ± 25.33 μm (Biofloat), compared to 5D plates (239.6 ± 9.06 μm), micromolds (265.3 ± 37.45 μm), and microtissue (417.8 ± 15.62 μm) (Figure 4E). Low attachment methods resulted in clear development of the necrotic core seen with propidium iodide staining (Figure S23A). This difference in cell viability is expected to attenuate oxygen diffusion through the media, which in turn can be affected by O_2 partial pressure, O_2 consumption rates, height of the culture to cell distance, temperature, and O_2 solubility.[92,93] Furthermore, nutrients become depleted, and waste products accumulate faster with a larger number of spheroids within the same volume and therefore require more frequent media exchange.

The spherical plate 5D spheroids showed lower oxygenation at the periphery (Figure S23B) and core (Figure 4C) compared to the microtissue (respectively $P = 0.013$ and $P > 0.9999$) and the self-made micromolds (respectively $P = 0.0007$ and $P = 0.0010$). This can be explained by the greater distance from the spheroid to the surface, leading to slower O_2 delivery in the static culture. This hypothesis is valid, as oxygenation in Biofloat and Lipidure low attachment plates are statistically similar. As we have seen previously, size differences between the high throughput methods cause significant differences in overall spheroids oxygenation (Figure 4D) but not in their steepness (Figure S23C). Most surprisingly, the low-attachment spheroids displayed increased oxygenation in their core, depending on their size and time after formation (Figure S24).

Thus, the MMIR1 probe demonstrated utility in monitoring cell oxygenation in dependence on the spheroid size, extracellular medium viscosity, and composition. In addition, the different spheroid formation methods can lead to drastic differences in spheroid composition and viability, agreeing with earlier studies and meta-analysis.[79]

Inverted O_2 Gradient in Spheroids. With some spheroid preparations, produced with, e.g., low-attachment methods (Figure 4B), we encountered an unusual "inverted gradient" distribution of hypoxia, when O_2 in the core was somewhat higher than at the periphery. Interestingly, this phenomenon was observed with spheroids produced from cell lines of completely different origins, including hDPSCs (stem cell line) and colon cancer HCT116 cells (Figures 5 and S25). Thus, with hDPSCs, small size spheroids showed "classical" O_2 distribution, while upon growing to larger sizes or when seeded with higher cell numbers (160 μm size, Figure 5A−C), the shape of the gradient changed. A similar situation was observed with HCT116 cells, although with spheroids of a much larger size (Figure 5D−F).

This phenomenon agrees with earlier studies performed by Sutherland and co-workers, which used microelectrode-based O_2-sensing in mouse epithelial breast cancer EMT6/Ro[94] and human colon adenocarcinoma Co112 spheroids.[24] Thus, a reversed correlation between central pO_2 and glucose supply in large spheroids (>900 μm) was reported. This suggests the potential metabolic adaptation of cells to the different microenvironmental conditions,[94] occurring in the vicinity of a necrotic core in large-size spheroids (Figure S26). Other studies using indirect hypoxia labeling with Pimonidazole, also reported a circular-shaped hypoxic area adjacent to the necrotic core in T-47D human breast cancer spheroids at day 8.[95]

Furthermore, we investigated the cellular metabolism using the autofluorescence of reduced nicotinamide adenine (phosphate) dinucleotide (NAD(P)H), involved in glycolysis and oxidative phosphorylation.[89,96] Its fluorescence lifetime is significantly shorter in its free state (~0.45 ns) compared to the protein-bound and other states.[97] Using low-attachment and micromold spheroid formation methods and various cell seeding densities, we looked at the development of an inverted oxygen gradient in spheroids from HCT116 cells.[98] First, using oxygenation analysis, we confirmed that spheroids from the two different size populations developed two distinct oxygenation profiles: generally hypoxic ("forward gradient" spheroids) and with pronounced "inverted" gradients (Figure S27A). Subsequently, we analyzed the spheroids with "forward" and "inverted" gradients (identified by oxygen microscopy) via two-photon NAD(P)H-FLIM. We observed a heterogeneous population of spheroids with "uniform" NAD(P)H fluorescence lifetime distribution (the most abundant in the group) and with "structured" NAD(P)H lifetime distribution (glycolytic core; less abundant) in a group of "small" size spheroids (Figures 6, 7A, S27B,C and ST3). The NAD(P)H-distribution structure heterogeneity of the small spheroid population agreed with our oxygenation data, where an appearance of inverted gradients was revealed by O_2 analysis (Figure S27A,B).

With the increase in spheroid size, we witnessed the formation of massive glycolytic core regions within spheroids with clearly shorter (blue) fluorescence lifetimes (Figures 6 and 7B). Thus, some spheroids demonstrated a large glycolytic core, occupying almost half of the spheroid and asymmetrically located close to the spheroid periphery (see example on Figures 6 bottom panel and S27C). A similar asymmetry was observed with spheroids having "inverted" oxygenation gradients, allowing us to speculate that both methods reveal similar metabolic layers in spheroids and that there is indeed a link between the metabolic stratification and oxygenation profiles within spheroids (Figure S27A).

We further looked at the spheroid size-dependent distribution of NAD(P)H lifetimes using "gold standard" phasor plot analysis (Figures S27 and 7) and demonstrated the appearance of shorter NAD(P)H fluorescence lifetime population in spheroids with "inverted" gradients, reflecting their complex metabolic organization. The 3D reconstruction

https://doi.org/10.1021/acsnano.3c12539
ACS Nano 2024, 18, 12168−12186

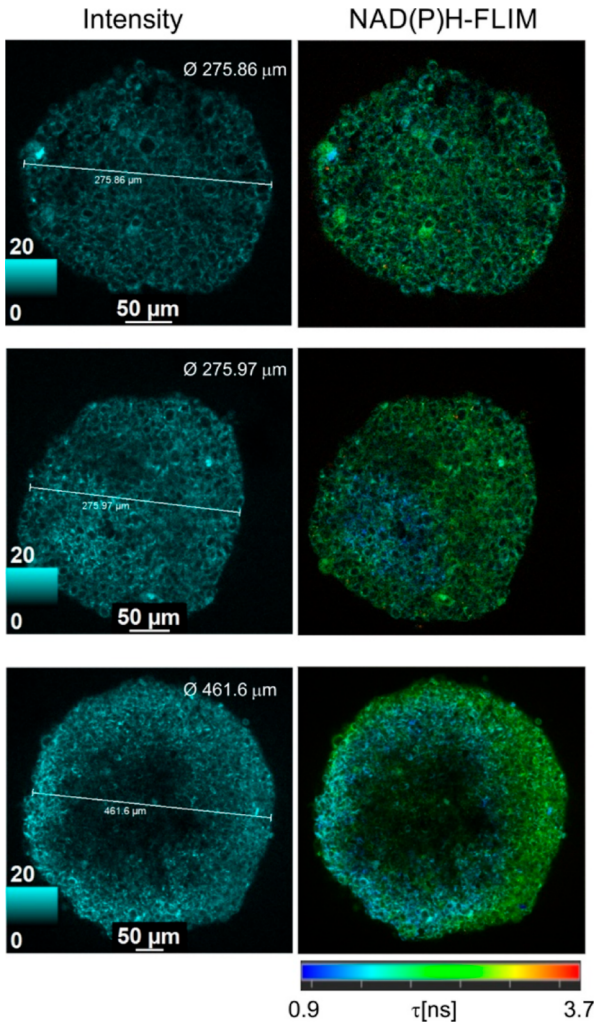

Figure 6. Examples of two-photon NAD(P)H-FLIM microscopy of HCT116 spheroids of different sizes (increase from top to bottom). Single optical sections (normalized intensity and fast-FLIM images) are shown. Scale bar is 50 μm.

of NAD(P)H autofluorescence in spheroids using phasor-FLIM false-color mask (Figure 7A,B) illustrates this observation on the example of spheroids with the small (from "forward" gradient spheroid population) and large (from "inverted" gradient spheroid population) glycolytic cores. The spheroid with a large glycolytic core (Figure 7B) displayed a phasor plot cloud with the appearance of short component lifetimes in comparison to the cloud of the spheroid with a small glycolytic core, where the shift toward the long lifetime component was observed. The statistical analysis of phasor plots from the "forward" and "inverted" gradient spheroid groups confirmed the difference between NAD(P)H fluorescence lifetimes, where the position of phasor plot cloud centroids (the linear alignment was detected with R^2 = 0.96, Figure 7D) in the "inverted" gradient spheroid group was closer to the theoretical position of monoexponential free-NAD(P)H phasor plot cloud with an average lifetime 0.45 ns (Figure 7C). These data confirm the dependence of observed fluorescence lifetimes on the metabolic status of cells in HCT116 cells.

Altogether, analysis of forward (normal) O_2 gradients and NAD(P)H-FLIM indicated the presence of a glycolytic core, which would progressively increase with the size and spheroid growth time. Interestingly, with increasing spheroid size (>300−500 μm), this core would also show shorter NAD(P)H intensities, pointing at a further decrease in metabolic activity and cell death. Figure 7E schematically shows a possible explanation of this phenomenon: we hypothesize that spheroids with a "homogeneous" distribution of their metabolically active cells (relying either on OxPhos, glycolysis, or a mixture of both) display a conventional "direct" O_2 gradient, determined mainly by diffusion and size. However, spheroids having distinct populations of metabolism will display a more complex oxygenation gradient. This working hypothesis points to the process of spontaneously organized cell metabolic "differentiation", which can occur with some cell lines in the spheroid cultures dynamically. We observed such a phenomenon only with certain cell lines and suspect that the formation of an inverted gradient can be a temporary process, leading to further cell death or further cell differentiation within the 3D cell "monoculture".

The observed formation of the glycolytic core in the spheroids and the resulting O_2 gradient were not reported in the literature previously.[99,100] This can be explained by the fact that most studies of tumor spheroids focused on these methods separately, often used lower-resolution equipment, and rarely looked at 3D context.[99,101−103] In addition, technical limitations of FLIM and PLIM microscopes available on the market[42,104] rarely allow for such experiments.

CONCLUSIONS

In this study, we produced deep-red/NIR dual emission nanosensor probes MMIR, which show reliable O_2 quantification in ratio-intensity and decay time readouts. Using the polymeric shell with either cationic or anionic resulting NPs displays cell-specific uptake through mixed-endocytosis with endo- and lysosomal localization, in agreement with our earlier studies with other reference and O_2-sensing dyes.[47,61] Within the optimized loading concentrations and incubation times, MMIR probes showed brightness and photostability, ensuring reliable quantification of hypoxia in monolayer and multicellular spheroid cell cultures with no cytotoxic effects (Figures 1 and 2). The observed slow cell uptake process (12−16 h) also results in slower release from the cells, which can enable long-term oxygenation monitoring in spheroid cultures for up to 21−26 days.

To illustrate the applicability of the produced nanosensor probe, we focused on "semiquantitative" ratiometric microscopy, which is widely available, in contrast to the PLIM method.[42,97] The described approach can be performed on conventional widefield LED-based fluorescence and laser-scanning confocal microscopes and macroimagers, with a detection sensitivity window of 600−800 nm. While the precise calibration and conversion of fluorescence ratio values into actual O_2 levels can pose technical challenges for multicellular spheroids and other 3D tissue models,[63,70,97,105,106] it offers real-time and reproducible analysis of ratios, contrasting with the end-point quantification methods.[42]

Collectively, our measurement approach applied to spheroids produced from both stem and cancer cells proved that the oxygenation gradients are not always static. The oxygenation gradients depend upon multiple factors, including spheroid size, extracellular viscosity, and spheroid formation and handling methods. This emphasizes the importance of oxygenation monitoring in studies involving the development

https://doi.org/10.1021/acsnano.3c12539
ACS Nano 2024, 18, 12168−12186

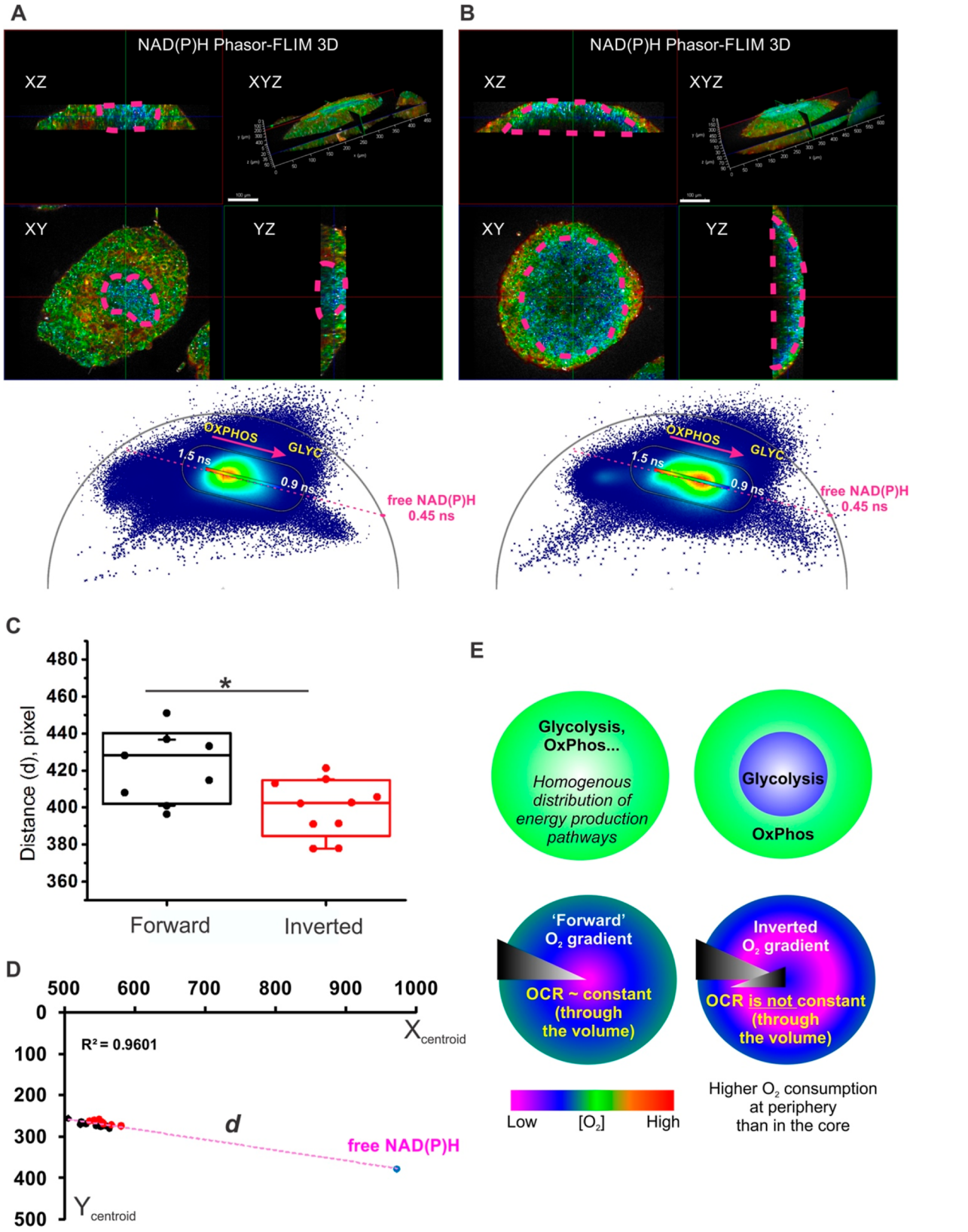

Figure 7. Two-photon FLIM of NAD(P)H reveals a glycolytic switch in HCT116 spheroids with "direct" and "inverted" oxygen gradients. (AB) 3D reconstructions of phasor-FLIM in 3D of early and mature spheroids with "inverted" gradient phenotype. The "glycolytic core" (demarcated by a purple dashed line) demonstrated local homogeneity of shorter NAD(P)H lifetime and was surrounded by a zone with longer lifetime distribution. Combined phasor plots of sections from 3D stack of spheroid from the "inverted" gradient group display a characteristic shift toward monoexponential free-NAD(P)H lifetime (0.45 ns) (magenta arrow). Scale bar is 100 μm. (C) Comparison of distances (d) between the theoretical position of phasor plot of free-NAD(P)H and centroids of free-NAD(P)H phasor plots of spheroids from "forward" and "inverted" gradient groups. Analyzed phasor plots corresponded to individual *XYZ* sections of spheroids imaged within

https://doi.org/10.1021/acsnano.3c12539
ACS Nano 2024, 18, 12168−12186

Figure 7. continued

~100−200 μm depth from the top of the spheroid. *T*-test ($P < 0.05$; *n* "forward" gradient spheroids is 7; *n* "inverted" gradient spheroids is 9) revealed a significant difference between groups, with the shift of phasor coordinates from "inverted" gradient group spheroids toward the free-NAD(P)H lifetime. Boxes represent standard deviation, and whiskers represent 10 and 90 percentiles. (D) Linear fitting of phasor plot centroids and free NAD(P)H theoretical coordinates demonstrated accurate linear alignment with $R^2 = 0.96$. (E) Hypothetical metabolic rearrangements in spheroids during the formation of "inverted" O_2 gradients.

and validation of targeted drug-/radiotherapies with cancer cells, tumor organoids, and "tumor avatars".[107,108] On the other hand, spheroids used as tissue building blocks in 3D printing, bioassembly, and biofabrication also require monitoring of their viability, cell death, and oxygenation.[109,110] Our "discovery" of the inverted oxygenation gradients with the presented approach and its correlation with autofluorescence label-free two-photon FLIM highlights the utility of the method, as more affordable, direct, and highly compatible with other multi-parameter micro- and mesoscopy modalities of 3D tissue models.

METHODS

Materials. PMMA-MA (10% methacrylic acid, MW ~ 100,000 Da, 17,913−500) was obtained from Polysciences (USA), organic solvents were obtained from Carl Roth (Austria), and Eudragit RL-100 polymer (~10% of quaternary ammonium groups, MW ~ 150,000 Da) was obtained from Degussa (33434-24-2, Degussa, Germany).

Standard cell culture plasticware was obtained from VWR (Belgium). For microscopy, cells were grown or were transferred (as spheroids) onto microscopy dishes (coverglass with no. 1.5 thickness, e.g. μ-slide 12-well, Ibidi GmbH, Germany, or equivalent) precoated with of 0.07 mg/mL collagen IV/0.03 mg/mL poly-D-lysine. The following dyes were used: Calcein Green AM (AS-89201, Tebubio, France), Sytox Green (S7020, Invitrogen, Belgium), Hoechst 33342 (H3570, Invitrogen, Belgium), LysoTracker Green DND-26 (L7526, Invitrogen, Belgium), MitoTracker Green (M7514, Invitrogen, Belgium), propidium iodide (25535-16-4, Sigma-Aldrich, Belgium), cholera toxin subunit B (Recombinant) Alexa Fluor 488 Conjugate (C34775, Invitrogen, Belgium), and tetramethylrhodamine, methyl ester (TMRM) dye (T668, Invitrogen, Belgium). The following viability assay kits were used: CellTiter-Glo Luminescent Cell Viability assay (G7571, Promega, Belgium), CellTiter 96 aqueous non-radioactive cell proliferation assay (G5421, Promega, Belgium), and CellTiter 3D cell viability assay (G9682, Promega, Belgium). Normalization of the ATP assays was done by a Pierce BCA protein assay kit (23,227, Thermo Fisher Scientific Inc., Belgium). The following mitochondrial drugs were used: FCCP (Sigma-Aldrich C2920-10MG, Belgium), oligomycin A (75351, Sigma-Aldrich, Belgium), Rotenone (R8875-1G, Sigma-Aldrich, Belgium), and Antimycin A (A8674−25MG, Sigma-Aldrich, Belgium).

Spheroids were formed using the following methods: 0.5 wt % Lipidure-CM5206 (AMS.52000034GB1G, Amsbio, UK) coating on a U-bottom 96-well plate (10062-900, VWR, Belgium), BIOFLOAT (83.3925.400, Sarstedt, Belgium), 3D Petri Dish micromolds (Z764000-6EA, MicroTissue Inc., USA), sphericalplate 5D 24-well (SP5D-24W, Kugelmeiers, Switzerland), and micropatterned 3D-printed PDMS stamps[63] producing 1589 spheroids per mold (provided by the Centre for Microsystems Technology, J. Vanfleteren, Ghent University).

Other reagents included glucose oxidase (250 μg/mL), KH_2PO_4 (4873, Merck, Belgium), Na_2SO_3 (239321-500G, Sigma-Aldrich, Belgium), 69 kDa dextran (D-1537 Sigma-Aldrich, Belgium), HEPES-Na (25249, Serva Electrophoresis, Germany), NaCl (CL00.1429.100, Chemlab, Belgium), EDTA (E5134-100G, Sigma-Aldrich, Belgium), 1% Igepal (CA630, Sigma-Aldrich, Belgium), and protease inhibitor cocktail (D2714, Sigma-Aldrich, Belgium).

Design and Characterization of the NP Probes. Oxygen indicator platinum(II) meso-tetra(4-fluorophenyl)-tetrabenzoporphyrin (PtTPTBPF)[72] was prepared via the template method reported by Hutter et al.[111] The reference dye (BF2 chelate of (3,5-diphenyl-1*H*-pyrrol-2-yl)(3,5-diphenylpyrrol-2-ylidene)-amine) "aza-BODIPY" was synthesized according to the published protocol.[74] ^{1}H NMR spectra for both dyes are provided in Supporting Information (Figures S1 and S2). The NPs were prepared as described previously.[71] Briefly, the dyes and the polymer were dissolved in organic solvent (acetone for RL-100 and acetone: tetrahydrofuran (9:1 v/v) for PMMA-MA, 0.2 wt % solution in both cases), and a 5× volume of deionized water was added rapidly (1−2 s) under vigorous stirring. The organic solvents were removed under reduced pressure.

Luminescence spectra were recorded on a Fluorolog-3 luminescence spectrometer (Horiba, Germany) equipped with a NIR-sensitive R2658 photomultiplier (Hamamatsu, Germany). The measurements were performed in 10 mm screw-capped quartz cuvettes (Starna Scientific, UK). Oxygen concentration was adjusted by bubbling nitrogen (99.999% purity, Air Liquide, Austria) or its mixture with compressed air through the dispersion of the particles. The gas mixtures were obtained using mass-flow controllers from Voegtlin (Switzerland, red-y smart series). The concentration of particles was adjusted to ~50 mg/L to avoid an inner filter effect. To investigate the effect of serum on the luminescence, the dispersions containing 10% volume of serum were measured in the same cuvette (Starna Scientific, UK). To avoid foam formation, oxygen concentrations were adjusted by introducing the gas mixtures for 1 h into the headspace of the cuvette and stirring the solution with a magnetic stirring bar.

Luminescence decay times were measured on the same spectrometer in time domain mode using a 455 nm SpectraLED (Horiba, Germany) as an excitation source (for phosphorescence of PtTPTBPF) or 635 nm NanoLED (Horiba, Germany) as an excitation source (for fluorescence of aza-BODIPY) and a DeltaHub module (Horiba, Germany). Data analysis was performed on DAS-6 Analysis software from Horiba.

Transmission Electron Microscopy. Morphology and size distribution were investigated for the three production batches of MMIR1 and MMIR− by drop casting (20 μg/mL, 2 μL) and dried overnight on Formvar/Carbon-coated hexagonal copper mesh grids (FCF200H-CU-TB, Electron Microscopy Sciences). The grids were observed on a JEM 1010 TEM (Jeol, Ltd., Japan) equipped with a charge-coupled device side-mounted Veleta camera (Emsis, Germany). NP size was measured manually using ImageJ software (NIH, USA).

NP Tracking Analysis. Nanoparticle tracking analysis (NTA) was performed for the three batches of MMIR1 and MMIR− using a NanoSight LM10-HS microscope (NanoSight, Amesbury, UK) equipped with a 45 mW 488 nm laser and an automatic syringe pump system. Three 30 s videos were recorded of each sample with camera levels of 13 (for MMIR−) and 15 (for MMIR1), a detection threshold of 3, and a syringe pump infusion speed of 20. Temperatures were monitored throughout the measurements; we assumed a medium viscosity of 0.929 cP, and the videos were analyzed with NTA software 3.4. For optimal measurements, the samples were diluted with Milli-Q water until the particle concentration was within an optimal concentration range of the NTA Software ($3 \times 10^8 - 1 \times 10^9$ particles/mL). All size distributions determined with NTA correspond to the hydrodynamic diameters of the particles in suspension.

https://doi.org/10.1021/acsnano.3c12539
ACS Nano 2024, 18, 12168−12186

Table 1. Image Acquisition Widefield Fluorescence Inverted Microscope (Olympus)

dye	light source	excitation filter (nm)	emission filter (nm)	exposure time (ms)	power (%)	objective
HXT 33342	405 nm	391−437	420−460	2	50	UPlanFL N 40×/0.6 air
Sytox Green	470 nm	460−495	510−550	10	50	UPlanFL N 40×/0.6 air
MMIR1 (reference)	580 nm	545−580	610 nm long-pass	20	25	UPlanFL N 40×/0.6 air
MMIR1 (O_2 sensitive)	635 nm	none/685 nm long-pass	705−845 nm	20	25	UPlanFL N 40×/0.6 air
Calcein Green-AM	490 nm	460−495	510−550	20	50	UPlanFL N 40×/0.6 air
Propidium iodide (PI)	550 nm	545−580	610 nm long-pass	25	25	UPlanFL N 40×/0.6 air
TMRM	550 nm	545−580	610 nm long-pass	5	25	UPlanFL N 20×/0.45
NADPH[113]	460 nm	460−495	510−550	120	25	UPlanFL N 40×/0.6 air
FAD	460 nm	460−495	510−550	40	50	UPlanFL N 40×/0.6 air

Cell Culture. Human colon cancer HCT116, human pancreatic cancer PANC1, human embryonic kidney cells HEK-293T, and ovarian cancer SKOV3 were obtained from the Laboratory of Experimental Cancer Research, Ghent University. Epithelial breast cancer MCF7 cell line was obtained from Radiobiology lab, Ghent University. HCT116 wild type and HCT116 $SCO_2^{-/-}$ cell lines[98] were kindly provided by P. Hwang (Cardiovascular and Cancer Genetics, National Institutes of Health). hDPSCs (PT-5025) and HUVECs (C2519A) were obtained from Lonza (Belgium). A short tandem repeat (STR) showed differences in both obtained HCT116 cell lines, compared to the ATCC one (Table S1). Therefore, "HCT116 ODW" (from LECR and ATCC) and "HCT116 Hwang" (NIH) are treated as separate cell lines. All presented data were produced with an HCT116 ODW cells, until otherwise mentioned. All cell lines were cultured in the recommended medium (Table S2) and under standard conditions, i.e., a humidified atmosphere of 37 °C, 18.6% O_2, and 5% CO_2. At 80−90% confluency, cells were passaged using 0.25% trypsin/EDTA (25,300,104, Gibco, USA) solution. Cells were cultured and analyzed under antibiotic-free conditions. Cells were regularly tested for lack of mycoplasma contamination using PCR (Eurofins Genomics).

Spheroid Formation Methods. HCT116 spheroids (initial concentration 500 cells per spheroid) were seeded with or without (for unstained samples) addition of 10 μg/mL MMIR1 on the low-attachment methods: 0.5 wt % Lipidure-CM5206 coating on a U-bottom 96-well plate, or BIOFLOAT and the high throughput-methods 3D Petri Dish micromolds producing 81 spheroids per mold, spherical plate 5D 24-well producing 750 spheroids per mold, and micropatterned 3D-printed PDMS stamps[63] producing 1589 spheroids per mold. Spheroid formation was performed over 5−6 days before transferring on a microscopy dish, counter-staining, and microscopy.

Evaluation of MMIR NPs with Monolayer Cell Cultures. 2D cultures were seeded on microscopy dishes at a density of 12,500−50,000 cells/well and incubated overnight for attachment. Loading of 2D cells with the oxygen sensing probes was typically performed by probe addition of 5−20 μg/mL incubation (17 h) in triplicate in a 5% CO_2 incubator at 37 °C, followed by washing (3×) with growth medium prior to microscopy and other experiments. For intracellular localization, HCT116 cells were stained with MMIR probes (5−20 μg/mL, overnight), followed by 1 h costaining with 25 ng/mL Calcein Green-AM, 100 nM MitoTracker Green FM, 200 nM LysoTracker Green DND-26, 2 nM HXT33342, or 2 μM Cholera Toxin Subunit B (Recombinant) Alexa Fluor 488 Conjugate, washing, and imaging on a confocal microscope.

Assessment of Cytotoxicity. The cytotoxicity effects of various concentrations of NPs for 2D cultures were investigated by costaining with 30 nM Sytox green and 0.5 μM Hoechst 33342 (1 h), washing, and imaging on a widefield fluorescence inverted microscope IX81 (Olympus). Viability effects on the membrane integrity were calculated by dividing $N_{\text{viable cells}}$ by the total cell number (viable + dead cells). Effects on total cell ATP (resting and metabolic stimulation) were probed using CellTiter-Glo Luminescent Cell Viability assay (Promega), according to the manufacturer's protocol with the luminescence recorded using the Spark multimode microplate reader (Tecan Spark 20M). Luminescence data on ATP were normalized by extracting the total cell protein with PEB buffer (50 mM HEPES-Na, pH 7.4, 150 mM NaCl, 1 mM EDTA, 1% Igepal CA630) and protease inhibitor cocktail and analyzed with Pierce BCA protein assay kit as described previously.[112]

Viability of 2D cell cultures was also studied using colorimetric 3-(4,5-dimethylthiazol-2-yl)-5-(3-carboxymethoxyphenyl)-2-(4-sulfophenyl)-2H-tetrazolium (MTS) assay (CellTiter 96 aqueous non-radioactive cell proliferation assay), according to the manufacturer's protocol, with the absorbance at 490 nm read using Universal Microplate Reader EL800 (Bio-TEK Instruments, Inc., USA). Linearity of response was investigated by seeding cells over the range of 64,000−2000 cells/well. For all 2D viability studies, 30,000 cells/well were seeded.

Cytotoxicity effects on MMIR-stained spheroids were investigated using the CellTiter 3D cell viability assay. Briefly, HCT116 spheroids were formed on 3D Petri Dish micromolds, at a density of 500 cells/well, and grown for 5 days. During formation, 20 μg/mL of MMIR1 was added to 10 replicates. Once formed, spheroids were transferred into a 96-well flat bottom plate coated with 0.07 mg/mL collagen IV/0.015 mg D-poly lysine and allowed to attach for 2 h. CellTiter-Glo 3D reagent was added in equal amounts of cell culture medium, and lysis was done by shaking for 5 min. After stabilizing the luminescent signal for 25 min, the signal was read using the Spark multimode microplate reader (Tecan Spark 20M) with an integration time of 1 s per well. Results were normalized by spheroid size (area square) division. Unstained and stained spheroids were also tested for differences in their NAD(P)H using two-photon microscopy (Figure S7).

Fluorescence Microscopy. *Widefield Fluorescence Microscopy.* Fluorescence microscopy was performed on a widefield fluorescence inverted microscope IX81 (Olympus), with motorized *Z*-axis control, CoolLED pE4000 (16 channels, 365−770 nm), an ORCA-Flash4.0LT+ (Hamamatsu) cMOS camera, glass warming plate Okolab, CellSens Dimension v.3 software, and air objectives 40×/0.6 UPlanFL N and 20×/0.45 UPLanFL N. The CellSens dimension (Olympus) software was used for imaging acquisition and processing with fixed settings (Table 1).

Photostability of the NPs was investigated on live HCT116 spheroids using the widefield fluorescence microscope IX81 (Olympus). The photostability was estimated by calculating the percentage of the reference intensity after 10 cycles of illumination for 10 spheroids. 10 nM of orange-red mitochondrial TMRM dye was used as a reference. Kinetic responses to mitochondrial stimuli on 5 days old HCT116 spheroids (formed microtissue molds, 500 cells per spheroid) were investigated by sequential treatment with mitochondrial uncoupler FCCP (1 μM) and inhibitor Rotenone (1 μM). The ratio responses were further validated by treatment of HCT116 spheroids with rotenone (1 μM) and antimycin A (1 μM), followed by deoxygenation using glucose oxidase (250 μg/mL) and potassium sulfite solution containing 5 mg/mL KH_2PO_4 and 5 mg/mL Na_2SO_3.

To visualize oxygen gradients, ratiometric analysis the following formula was used: $R = \frac{I_{\text{reference dye}} - I_{\text{reference background}}}{I_{\text{sensitive dye}} - I_{\text{sensitive background}}}$ for each pixel of the 3D model. Each "ratio pixel" was converted into a color gradient. We used the parameters "oxygen gradient" ($R_{\text{periphery}} - R_{\text{core}}$) and "steepness" (Δratio/spheroids radius) introduced previously.[63]

https://doi.org/10.1021/acsnano.3c12539
ACS Nano 2024, 18, 12168−12186

Size-dependent oxygenation: HCT116 cells were prestained with a 10 μg/mL MMIR1 probe overnight before spheroid formation on 0.5 wt % Lipidure 96-well plates with addition of 1 μg/mL MMIR1 in multiple seeding densities (500, 1000, 5000, and 10,000 cells per well) in 6 replicates. Line profiles were taken by using the "line profile" tool with CellSens software (Olympus).

Effect of medium on oxygenation: To investigate the effects of increased viscosity and glucose concentration on the oxygen gradient in live HCT116 spheroids, culture media was exchanged with imaging media with either D-glucose (0−25 mM) or 0 to 5%w/w 69 kDa dextran resulting in a viscosity ranging from 0.7748 to 2.25 cP at 37 °C, 4 h before imaging.[114] HCT116 spheroids were formed using the high throughput agarose micromold method with the addition of MMIR1 (10 μg/mL) and grown for 5 days.

Inverted oxygenation gradient analysis: Live DPSCs spheroids were formed by seeding 300,000 and 1.300,000 cells/mL on a micropatterned agarose-coated tissue culture plate.[63] Theoretically, the cells were then equally distributed among the 1585 microwells, resulting in 189 and 820 cells per spheroid, respectively. Live HCT116 spheroids were formed by seeding 500, 1000, 10,000, and 20,000 cells per spheroid in a Lipidure-coated plate (Amsbio). After 7 days (HCT116) and 8 days (DPSCs) of CO_2 incubation at 37 °C, spheroids were transferred to precoated microscopy dishes. Multiparametric analysis was performed by PI staining (1 μg/mL, 1 h), NAD(P)H-specific fluorescent probe[113] (20 μM, 1 h), and FAD autofluorescence (exc. 460 nm, 510−550 nm emission) on the Olympus IX81 microscope.

Confocal FLIM microscopy was performed on an inverted Stellaris 8 Falcon (Leica) microscope (Ghent Light Microscopy Core), equipped with the white-light laser (440−790 nm), HC PL Apo 10×/0.4 air, HC Fluotar 25×/0.95 W, HC PL Apo 40×/1.25 GLYC corr., HC PL Apo 63×/1.4 oil objectives, HyD X, HyD R and HyD S detectors, temperature-controlled incubator, and dedicated LAS X acquisition and analysis software (ver. 4.6.0), as described previously.[115] For colocalization studies, typically 40×/1.25 GLYC corr. objective was used, with MMIR excited at 614 nm (4.34%), emission collected at 639−696 nm (reference channel, HyD X3 detector) and 724−780 nm (O_2-sensitive channel, HyD R detector), pixel dwell time 4.1 μs, and 1024 × 1024 resolution. Counter-stains were imaged according to their spectral settings.

Two-photon FLIM microscopy was performed on an inverted Dive SP8 Falcon (Leica) microscope, equipped with IR Mai Tai HP laser (690−1040 nm), a temperature-controlled incubator, HC Fluotar 25×/0.95 W objective, and dedicated LAS X acquisition and analysis software. NAD(P)H was excited at 740 nm (20% laser power) with emission collected at 420−470 nm, at 512 × 512 resolution, and pixel dwell time 3.2 μs. Produced images were analyzed using LAS X FLIM analysis suite for reconstructing 3D FLIM and phasor FLIM images. NAD(P)H-FLIM-based analysis of OxPhos/Glycolysis states in spheroids was done by comparing the shift of the NAD(P)H phasor plots of spheroids from the theoretical position of monoexponential free-NAD(P)H lifetime (~0.45 ns)[116] on the universal circle. Threshold 5 wavelet filter was applied for phasor plots corresponding to individual spheroid ROIs, and the theoretical position of free-NAD(P)H lifetime on a universal circle was determined in LAS X-FLIM software. Phasor plots were exported as TIFF files (600 × 1024 pixels) together with the circular mask and free-NAD(P)H position. Narrowed phasor plot clouds and free-NAD(P)H position on a universal circle were selected in ImageJ[117] by application of corresponding threshold filters with fixed color space, brightness, and saturation parameters to generate corresponding ROI masks. The centroids of phasor plot masks were determined using the standard "measure" protocol, and their coordinates (in pixels), corresponding to their coordinates inside the universal circle, were exported in an excel table format. Distance (d) calculation between centroids and theoretical free-NAD(P)H position was performed using the Pythagorean formula

$$d = \sqrt{(x_f - x_c)^2 + (y_f - y_c)^2}$$

where x_f and y_f are coordinates of free-NAD(P)H and x_c and y_c are coordinates of phasor plot centroids. The linear alignment of centroids with free-NADPH was verified by linear fitting with a R^2 = 0.96.

DATA ASSESSMENT AND STATISTICS

2D cell staining studies were analyzed by averaging the intensity values of 10 randomly selected ROI per replicate. For spheroids, 10 ROIs at the periphery and 10 ROIs at the core were randomly selected. All MMIR application methods were performed in at least 3 independent experimental replicates to ensure reproducibility. All results are represented as mean values ±SEM. The number of replicates can be found in the legend of each figure. Figures were made by using Inkscape software. Quantitative data were analyzed, and graphs were made using GraphPad Prism 9. Normally distributed data were subjected to a Student's T-test or a one-way ANOVA. Alternatively, the nonparametric Mann−Whitney U test (two groups) or Kruskal−Wallis test (multiple groups) were performed. In the case of a significant result, the Tukey HSD test (parametric) or a pairwise comparison through the Wilcoxon rank sum test with Bonferroni correction was performed. Significant differences are shown as follows: * = $P < 0.05$, ** = $P < 0.01$, *** = $P < 0.001$ and **** = $P < 0.0001$.

ASSOCIATED CONTENT

Supporting Information

The Supporting Information is available free of charge at https://pubs.acs.org/doi/10.1021/acsnano.3c12539.

^{1}H NMR spectrum ($CDCl_3$, 400 MHz) of BF_2 chelate of (3,5-diphenyl-1H-pyrrol-2-yl)(3,5-diphenylpyrrol-2-ylidene)amine ("aza-BODIPY"), ^{1}H NMR spectrum (CD_2Cl_2, 400 MHz) of PtTPTBPF, normalized absorption spectra of the particles (1:1 wt ratio of the dyes) for 3 different batches of each type, emission spectra (λ_{exc} = 615 nm) of the particles (1:1 wt ratio of the dyes) for three different batches of each type, appearance of aqueous dispersions of the NPs (concentration 2 mg/mL), MMIR after 2 weeks storage at 4 °C, MMIR1 after ~2 years storage at 4 °C, MMIR− after 2 weeks storage at 4 °C, MMIR− after ~2 years storage at 4 °C, emission spectra of MMIR1 and MMIR− NPs (dye ratio 1:1) in anoxic water, absorption of both dispersions was identical at the excitation wavelength (615 nm), luminescence decays of the reference dye in MMIR1 and MMIR− beads (both 1:1 ratio of the dyes) monitored at 660 nm (λ_{exc} = 635 nm, NanoLED, Horiba; 23 °C), phosphorescence decay of PtTPTBPF in MMIR1 beads (1:1 ratio of the dyes) monitored at 760 nm (λ_{exc} = 456 nm, SpectraLED from Horiba; 23 °C), phosphorescence decay of PtTPTBPF in MMIR− beads (1:1 ratio of the dyes) monitored at 760 nm (λ_{exc} = 455 nm, SpectraLED from Horiba; 23 °C), NP size measurements of three production batches of MMIR1 and MMIR− using NanoSight (A) and TEM (B) methods, comparison of positively charged MMIR1 with different sensitive/reference dye ratios and negatively charged (1:1) MMIR− probe, fluorescence signals of MMIR1-stained HCT116 spheroids over 26 days period, intracellular localization of MMIR1 after overnight incubation with HCT116 cells (5 μg/mL, 17 h) shows endo- and lysosomal localization, cell line-

https://doi.org/10.1021/acsnano.3c12539
ACS Nano 2024, 18, 12168−12186

dependent uptake of the positive (RL100) and negative (PMMA) charged MMIR probes, prestaining of HCT116 cells overnight ensures uniform staining, addition of MMIR probes shows no significant cell death in monolayer and spheroids of HCT116 cells, viability assay using the CellTiter 96 aqueous non-radioactive cell proliferation assay (MTS, Promega) shows no cellular toxicity due to 24 h incubation of both cationic (MMIR1) and negatively charged (MMIR−) nanosensors with live HCT116 cells, two-photon FLIM of NAD(P)H shows no changes in cell redox (NAD(P)H fluorescence lifetimes) in response to MMIR1 addition to live HCT116 spheroids, dynamic response of MMIR probes to drugs affecting cell bioenergetics and deoxygenation, size-dependent oxygenation of live HCT116 cells spheroids, increased cell medium viscosity results in the formation of a more hypoxic core, decreased cell media glucose concentration does not affect spheroids oxygenation, formation methods affect the viability and oxygenation in live HCT116 spheroids, inverted gradient formation in live HCT116 spheroids is both time and size-dependent, analysis of "inverted" oxygenation gradient in live DPSCs and HCT116 spheroids, cell death comparison between "direct" and "inverted" gradients in DPSCs and HCT116 spheroids formed on respectively microagarose molds and Lipidure-coated plates, examples of two-photon NAD(P)H-FLIM microscopy and phasor plots of HCT116 spheroids with different sizes, STR authentication HCT116 cell lines, composition of used growth and imaging media, and morphological characterization of spheroid populations (PDF)

AUTHOR INFORMATION

Corresponding Authors

Sergey M. Borisov − *Institute of Analytical Chemistry and Food Chemistry, Graz University of Technology, Graz 8010, Austria;* orcid.org/0000-0001-9318-8273; Email: sergey.borisov@tugraz.at

Ruslan I. Dmitriev − *Tissue Engineering and Biomaterials Group, Department of Human Structure and Repair, Faculty of Medicine and Health Sciences, Ghent University, 9000 Ghent, Belgium; Ghent Light Microscopy Core, Ghent University, 9000 Ghent, Belgium;* orcid.org/0000-0002-0347-8718; Email: Ruslan.dmitriev@ugent.be

Authors

Angela C. Debruyne − *Tissue Engineering and Biomaterials Group, Department of Human Structure and Repair, Faculty of Medicine and Health Sciences, Ghent University, 9000 Ghent, Belgium*

Irina A. Okkelman − *Tissue Engineering and Biomaterials Group, Department of Human Structure and Repair, Faculty of Medicine and Health Sciences, Ghent University, 9000 Ghent, Belgium; Ghent Light Microscopy Core, Ghent University, 9000 Ghent, Belgium*

Nina Heymans − *Tissue Engineering and Biomaterials Group, Department of Human Structure and Repair, Faculty of Medicine and Health Sciences, Ghent University, 9000 Ghent, Belgium*

Cláudio Pinheiro − *Laboratory of Experimental Cancer Research, Department of Human Structure and Repair, Ghent University, 9000 Ghent, Belgium; Cancer Research Institute Ghent (CRIG), 9000 Ghent, Belgium*

An Hendrix − *Laboratory of Experimental Cancer Research, Department of Human Structure and Repair, Ghent University, 9000 Ghent, Belgium; Cancer Research Institute Ghent (CRIG), 9000 Ghent, Belgium*

Max Nobis − *Intravital Imaging Expertise Center, VIB Center for Cancer Biology, KU Leuven, 3000 Leuven, Belgium;* orcid.org/0000-0002-1861-1390

Complete contact information is available at: https://pubs.acs.org/10.1021/acsnano.3c12539

Notes

The authors declare no competing financial interest.

The preprint version of this manuscript is available: Angela C. Debruyne, Irina A. Okkelman, Nina Heymans, Cláudio Pinheiro, An Hendrix, Max Nobis, Sergey M. Borisov, and Ruslan I. Dmitriev. Live microscopy of multicellular spheroids with the multimodal near-infrared nanoparticles reveals differences in oxygenation gradients. bioRxiv 2023.12.11.571110; doi: 10.1101/2023.12.11.571110 (accessed 03-29-2024).

ACKNOWLEDGMENTS

We would like to thank O. De Wever and A. Baeyens (Ghent University) for sharing the cell lines, P. Hwang (National Institutes of Health) for HCT116 wild type and KO $SCO_2^{-/-}$ cell lines, M. Claeys (The Nematology Research Unit, UGent TEM Core Facility) for help with transmission the electron microscopy, D. Krysko and A. Labro (Ghent University) for support with a multimode microplate reader, C. Scheele (VIB, KU Leuven) for support with multiphoton microscopy, and M. Barroso lab (Albany Medical College) for discussions on 3D models and O_2 probes. This research was supported by the Special Research Fund (BOF) starting investigator grant (BOF/STA/202009/003), Research Foundation Flanders (FWO) grants (I001922N, K1D0222N, K1DKE23N, K207223N, K1DKX23N, and K1D6622N) and European Union, fliMAGIN3D-DN Horizon Europe MSCA-DN no. 101073507. This research was funded in part by the Austrian Science Fund (FWF) 10.55776/ P32079-N37. For the purpose of open access, the authors have applied a CC BY public copyright licence to any Author Accepted Manuscript version arising from this submission.

REFERENCES

(1) Borras, C. Relevance of Oxygen Concentration in Stem Cell Culture for Regenerative Medicine. *Free Radicals Biol. Med.* **2021**, *165*, 4−5.

(2) Bilan, D. S.; Belousov, V. V. New Tools for Redox Biology: From Imaging to Manipulation. *Free Radicals Biol. Med.* **2017**, *109*, 167−188.

(3) Kunz, M.; Ibrahim, S. Molecular Responses to Hypoxia in Tumor Cells. *Mol. Cancer* **2003**, *2*, 23.

(4) Mazure, N. M.; Pouysségur, J. Hypoxia-Induced Autophagy: Cell Death or Cell Survival? *Curr. Opin. Cell Biol.* **2010**, *22* (2), 177−180.

(5) Miyamoto, O.; Auer, R. N. Hypoxia, Hyperoxia, Ischemia, and Brain Necrosis. *Neurology* **2000**, *54* (2), 362.

(6) Rodrigo, J.; Fernandez, A.; Serrano, J.; Peinado, M.; Martinez, A. The Role of Free Radicals in Cerebral Hypoxia and Ischemia. *Free Radicals Biol. Med.* **2005**, *39* (1), 26−50.

(7) Luo, Z.; Tian, M.; Yang, G.; Tan, Q.; Chen, Y.; Li, G.; Zhang, Q.; Li, Y.; Wan, P.; Wu, J. Hypoxia Signaling in Human Health and

Diseases: Implications and Prospects for Therapeutics. *Signal Transduction Targeted Ther.* **2022**, *7* (1), 218.
(8) Yu, B.; Wang, X.; Song, Y.; Xie, G.; Jiao, S.; Shi, L.; Cao, X.; Han, X.; Qu, A. The Role of Hypoxia-Inducible Factors in Cardiovascular Diseases. *Pharmacol. Ther.* **2022**, *238*, 108186.
(9) Pham, K.; Parikh, K.; Heinrich, E. Hypoxia and Inflammation: Insights From High-Altitude Physiology. *Front. Physiol.* **2021**, *12*, 676782.
(10) Taylor, C. T.; Colgan, S. P. Regulation of Immunity and Inflammation by Hypoxia in Immunological Niches. *Nat. Rev. Immunol.* **2017**, *17* (12), 774−785.
(11) Reyes, A.; Duarte, L. F.; Farías, M. A.; Tognarelli, E.; Kalergis, A. M.; Bueno, S. M.; González, P. A. Impact of Hypoxia over Human Viral Infections and Key Cellular Processes. *Int. J. Mol. Sci.* **2021**, *22*, 7954.
(12) Schaffer, K.; Taylor, C. T. The Impact of Hypoxia on Bacterial Infection. *FEBS J.* **2015**, *282* (12), 2260−2266.
(13) Thompson, A. A. R.; Dickinson, R. S.; Murphy, F.; Thomson, J. P.; Marriott, H. M.; Tavares, A.; Willson, J.; Williams, L.; Lewis, A.; Mirchandani, A.; Dos Santos Coelho, P.; Doherty, C.; Ryan, E.; Watts, E.; Morton, N. M.; Forbes, S.; Stimson, R. H.; Hameed, A. G.; Arnold, N.; Preston, J. A.; Lawrie, A.; Finisguerra, V.; Mazzone, M.; Sadiku, P.; Goveia, J.; Taverna, F.; Carmeliet, P.; Foster, S. J.; Chilvers, E. R.; Cowburn, A. S.; Dockrell, D. H.; Johnson, R. S.; Meehan, R. R.; Whyte, M. K. B.; Walmsley, S. R. Hypoxia Determines Survival Outcomes of Bacterial Infection through HIF-1α-Dependent Reprogramming of Leukocyte Metabolism. *Sci. Immunol.* **2017**, *2* (8), No. eaal2861.
(14) Rakotomalala, A.; Escande, A.; Furlan, A.; Meignan, S.; Lartigau, E. Hypoxia in Solid Tumors: How Low Oxygenation Impacts the "Six Rs" of Radiotherapy. *Front. Endocrinol.* **2021**, *12*..
(15) Parks, S. K.; Cormerais, Y.; Pouysségur, J. Hypoxia and Cellular Metabolism in Tumour Pathophysiology. *J. Physiol.* **2017**, *595* (8), 2439−2450.
(16) Saxena, K.; Jolly, M. K.; Balamurugan, K. Hypoxia, partial EMT and collective migration: Emerging culprits in metastasis. *Transl. Oncol.* **2020**, *13* (11), 100845.
(17) Hall, E. J.; Giaccia, A. J. *Radiobiology for the Radiologist*, 7th ed.; Lippincott Williams & Wilkins: Philadelphia, 2006; Vol. *6*.
(18) Bhattacharya, S.; Calar, K.; de la Puente, P. Mimicking Tumor Hypoxia and Tumor-Immune Interactions Employing Three-Dimensional in Vitro Models. *J. Exp. Clin. Cancer Res.* **2020**, *39* (1), 75.
(19) Fontana, F.; Raimondi, M.; Marzagalli, M.; Sommariva, M.; Gagliano, N.; Limonta, P. Three-Dimensional Cell Cultures as an In Vitro Tool for Prostate Cancer Modeling and Drug Discovery. *Int. J. Mol. Sci.* **2020**, *21*, 6806.
(20) Nunes, A. S.; Barros, A. S.; Costa, E. C.; Moreira, A. F.; Correia, I. J. 3D Tumor Spheroids as in Vitro Models to Mimic in Vivo Human Solid Tumors Resistance to Therapeutic Drugs. *Biotechnol. Bioeng.* **2019**, *116* (1), 206−226.
(21) Leek, R.; Grimes, D. R.; Harris, A. L.; McIntyre, A. Methods: Using Three-Dimensional Culture (Spheroids) as an In Vitro Model of Tumour Hypoxia. *Adv. Exp. Med. Biol.* **2016**, *899*, 167−196.
(22) Freyer, J. P.; Sutherland, R. M. Selective Dissociation and Characterization of Cells from Different Regions of Multicell Tumor Spheroids1. *Cancer Res.* **1980**, *40* (11), 3956−3965.
(23) Casciari, J. J.; Sotirchos, S. V.; Sutherland, R. M. Glucose Diffusivity in Multicellular Tumor Spheroids. *Cancer Res.* **1988**, *48* (14), 3905−3909.
(24) Sutherland, R. M.; Sordat, B.; Bamat, J.; Gabbert, H.; Bourrat, B.; Mueller-Klieser, W. Oxygenation and Differentiation in Multicellular Spheroids of Human Colon Carcinoma. *Cancer Res.* **1986**, *46* (10), 5320−5329.
(25) Riffle, S.; Hegde, R. S. Modeling Tumor Cell Adaptations to Hypoxia in Multicellular Tumor Spheroids. *J. Exp. Clin. Cancer Res.* **2017**, *36* (1), 102.
(26) Aubert, L.; Bastien, E.; Renoult, O.; Guilbaud, C.; Özkan, K.; Brusa, D.; Bouzin, C.; Richiardone, E.; Richard, C.; Boidot, R.; Léonard, D.; Corbet, C.; Feron, O. Tumor Acidosis-Induced DNA Damage Response and Tetraploidy Enhance Sensitivity to ATM and ATR Inhibitors. *EMBO Rep.* **2024**, *25*, 1469−1489.
(27) Mueller-Klieser, W. Method for the Determination of Oxygen Consumption Rates and Diffusion Coefficients in Multicellular Spheroids. *Biophys. J.* **1984**, *46* (3), 343−348.
(28) Krohn, K. A.; Link, J. M.; Mason, R. P. Molecular Imaging of Hypoxia. *J. Nucl. Med.* **2008**, *49* (Suppl 2), 129S−148S.
(29) Rademakers, S. E.; Lok, J.; van der Kogel, A. J.; Bussink, J.; Kaanders, J. H. A. M. Metabolic Markers in Relation to Hypoxia; Staining Patterns and Colocalization of Pimonidazole, HIF-1α, CAIX, LDH-5, GLUT-1, MCT1 and MCT4. *BMC Cancer* **2011**, *11* (1), 167.
(30) Bauer, N.; Maisuls, I.; Pereira da Graça, A.; Reinhardt, D.; Erapaneedi, R.; Kirschnick, N.; Schäfers, M.; Grashoff, C.; Landfester, K.; Vestweber, D.; Strassert, C. A.; Kiefer, F. Genetically Encoded Dual Fluorophore Reporters for Graded Oxygen-Sensing in Light Microscopy. *Biosens. Bioelectron.* **2023**, *221*, 114917.
(31) Kostyuk, A.; Kokova, A.; Podgorny, O.; Kelmanson, I.; Fetisova, E.; Belousov, V.; Bilan, D. Genetically Encoded Tools for Research of Cell Signaling and Metabolism under Brain Hypoxia. *Antioxidants* **2020**, *9*, 516.
(32) Dornhof, J.; Zieger, V.; Kieninger, J.; Frejek, D.; Zengerle, R.; Urban, G. A.; Kartmann, S.; Weltin, A. Bioprinting-Based Automated Deposition of Single Cancer Cell Spheroids into Oxygen Sensor Microelectrode Wells. *Lab Chip* **2022**, *22* (22), 4369−4381.
(33) Kann, S. H.; Shaughnessey, E. M.; Coppeta, J. R.; Azizgolshani, H.; Isenberg, B. C.; Vedula, E. M.; Zhang, X.; Charest, J. L. Measurement of Oxygen Consumption Rates of Human Renal Proximal Tubule Cells in an Array of Organ-on-Chip Devices to Monitor Drug-Induced Metabolic Shifts. *Microsyst. Nanoeng.* **2022**, *8* (1), 109.
(34) Gerencser, A. A.; Neilson, A.; Choi, S. W.; Edman, U.; Yadava, N.; Oh, R. J.; Ferrick, D. A.; Nicholls, D. G.; Brand, M. D. Quantitative Microplate-Based Respirometry with Correction for Oxygen Diffusion. *Anal. Chem.* **2009**, *81* (16), 6868−6878.
(35) Zhdanov, A. V.; Favre, C.; O'Flaherty, L.; Adam, J.; O'Connor, R.; Pollard, P. J.; Papkovsky, D. B. Comparative Bioenergetic Assessment of Transformed Cells Using a Cell Energy Budget Platform. *Integr. Biol.* **2011**, *3* (11), 1135−1142.
(36) Kiyose, K.; Hanaoka, K.; Oushiki, D.; Nakamura, T.; Kajimura, M.; Suematsu, M.; Nishimatsu, H.; Yamane, T.; Terai, T.; Hirata, Y.; Nagano, T. Hypoxia-Sensitive Fluorescent Probes for in Vivo Real-Time Fluorescence Imaging of Acute Ischemia. *J. Am. Chem. Soc.* **2010**, *132* (45), 15846−15848.
(37) Erapaneedi, R.; Belousov, V. V.; Schäfers, M.; Kiefer, F. A Novel Family of Fluorescent Hypoxia Sensors Reveal Strong Heterogeneity in Tumor Hypoxia at the Cellular Level. *EMBO J.* **2016**, *35* (1), 102−113.
(38) Nomata, J.; Hisabori, T. Development of Heme Protein Based Oxygen Sensing Indicators. *Sci. Rep.* **2018**, *8* (1), 11849.
(39) Akiyama, H.; Takahashi, I.; Shimoda, Y.; Mukai, R.; Yoshihara, T.; Tobita, S. Ir(III) Complex-Based Oxygen Imaging of Living Cells and Ocular Fundus with a Gated ICCD Camera. *Photochem. Photobiol. Sci.* **2018**, *17* (6), 846−853.
(40) Dmitriev, R. I.; Zhdanov, A. V.; Nolan, Y. M.; Papkovsky, D. B. Imaging of Neurosphere Oxygenation with Phosphorescent Probes. *Biomaterials* **2013**, *34* (37), 9307−9317.
(41) Grist, S. M.; Bennewith, K. L.; Cheung, K. C. Oxygen Measurement in Microdevices. *Annu. Rev. Anal. Chem.* **2022**, *15* (1), 221−246.
(42) Papkovsky, D. B.; Dmitriev, R. I. Imaging of Oxygen and Hypoxia in Cell and Tissue Samples. *Cell. Mol. Life Sci.* **2018**, *75*, 2963−2980.
(43) Dmitriev, R. I.; Borisov, S. M.; Dussmann, H.; Sun, S.; Müller, B. J.; Prehn, J.; Baklaushev, V. P.; Klimant, I.; Papkovsky, D. B. Versatile Conjugated Polymer Nanoparticles for High-Resolution O_2 Imaging in Cells and 3D Tissue Models. *ACS Nano* **2015**, *9*, 5275−5288.

https://doi.org/10.1021/acsnano.3c12539
ACS Nano 2024, 18, 12168−12186

(44) Okkelman, I. A.; Foley, T.; Papkovsky, D. B.; Dmitriev, R. I. Live Cell Imaging of Mouse Intestinal Organoids Reveals Heterogeneity in Their Oxygenation. *Biomaterials* **2017**, *146*, 86−96.
(45) Papkovsky, D. B.; Dmitriev, R. I. Quenched-Phosphorescence Detection of Molecular Oxygen: Applications in Life Sciences. In *Evolution of Cell-Penetrating Phosphorescent O2 Probes* Papkovsky, D. B., Dmitriev, R. I., Eds.; *RSC Detection Science*; The Royal Society of Chemistry, 2018; pp 50−70.
(46) Dussmann, H.; Perez-Alvarez, S.; Anilkumar, U.; Papkovsky, D.; Prehn, J. Single-Cell Time-Lapse Imaging of Intracellular O_2 in Response to Metabolic Inhibition and Mitochondrial Cytochrome-c Release. *Cell Death Dis.* **2017**, *8*, No. e2853.
(47) Kondrashina, A. V.; Dmitriev, R. I.; Borisov, S. M.; Klimant, I.; O'Brien, I.; Nolan, Y. M.; Zhdanov, A. V.; Papkovsky, D. B. A Phosphorescent Nanoparticle-Based Probe for Sensing and Imaging of (Intra)Cellular Oxygen in Multiple Detection Modalities. *Adv. Funct. Mater.* **2012**, *22* (23), 4931−4939.
(48) Wang, Y.; Qin, F.; Zhang, H.; Kou, M.; Zhang, Z. A High-Performance Optical Trace Oxygen Sensor Based on the Room-Temperature Phosphorescence from Palladium (II) Octaethylporphyrin. *Measurement* **2023**, *206*, 112275.
(49) Choi, N. W.; Verbridge, S. S.; Williams, R. M.; Chen, J.; Kim, J.-Y.; Schmehl, R.; Farnum, C. E.; Zipfel, W. R.; Fischbach, C.; Stroock, A. D. Phosphorescent Nanoparticles for Quantitative Measurements of Oxygen Profiles in Vitro and in Vivo. *Biomaterials* **2012**, *33* (9), 2710−2722.
(50) Wilson, D. F. Oxygen Dependent Quenching of Phosphorescence: A Perspective. *Adv. Exp. Med. Biol.* **1992**, *317*, 195−201.
(51) Papkovsky, D. B.; Dmitriev, R. I. Biological Detection by Optical Oxygen Sensing. *Chem. Soc. Rev.* **2013**, *42* (22), 8700−8732.
(52) Filatov, M. A.; Baluschev, S.; Landfester, K. Protection of Densely Populated Excited Triplet State Ensembles against Deactivation by Molecular Oxygen. *Chem. Soc. Rev.* **2016**, *45*, 4668−4689.
(53) Briñas, R. P.; Troxler, T.; Hochstrasser, R. M.; Vinogradov, S. A. Phosphorescent Oxygen Sensor with Dendritic Protection and Two-Photon Absorbing Antenna. *J. Am. Chem. Soc.* **2005**, *127* (33), 11851−11862.
(54) Roussakis, E.; Li, Z.; Nichols, A. J.; Evans, C. L. Oxygen-Sensing Methods in Biomedicine from the Macroscale to the Microscale. *Angew. Chem., Int. Ed.* **2015**, *54* (29), 8340−8362.
(55) Filatov, M. A. Chapter 5 Protection of Triplet Excited State Materials from Oxygen Quenching and Photooxidation in Optical Sensing Applications. In *Applications of Quenched Phosphorescence Detection of Molecular Oxygen in Life Sciences*; *RSC Detection Science*; Royal Society of Chemistry, 2018; .
(56) Fercher, A.; Borisov, S. M.; Zhdanov, A. V.; Klimant, I.; Papkovsky, D. B. Intracellular O2 Sensing Probe Based on Cell-Penetrating Phosphorescent Nanoparticles. *ACS Nano* **2011**, *5* (7), 5499−5508.
(57) Dmitriev, R. I.; Borisov, S. M.; Düssmann, H.; Sun, S.; Müller, B. J.; Prehn, J.; Baklaushev, V. P.; Klimant, I.; Papkovsky, D. B. Versatile Conjugated Polymer Nanoparticles for High-Resolution O_2 Imaging in Cells and 3D Tissue Models. *ACS Nano* **2015**, *9* (5), 5275−5288.
(58) Wu, C.; Bull, B.; Christensen, K.; McNeill, J. Ratiometric Single-Nanoparticle Oxygen Sensors for Biological Imaging. *Angew. Chem., Int. Ed. Engl.* **2009**, *48*, 2741−2745.
(59) Ashokkumar, P.; Adarsh, N.; Klymchenko, A. S. Ratiometric Nanoparticle Probe Based on FRET-Amplified Phosphorescence for Oxygen Sensing with Minimal Phototoxicity. *Small* **2020**, *16* (32), 2002494.
(60) Shi, H.; Ma, X.; Zhao, Q.; Liu, B.; Qu, Q.; An, Z.; Zhao, Y.; Huang, W. Ultrasmall Phosphorescent Polymer Dots for Ratiometric Oxygen Sensing and Photodynamic Cancer Therapy. *Adv. Funct. Mater.* **2014**, *24* (30), 4823−4830.
(61) Dmitriev, R. I.; Borisov, S. M.; Kondrashina, A. V.; Pakan, J. M. P.; Anilkumar, U.; Prehn, J. H. M.; Zhdanov, A. V.; McDermott, K. W.; Klimant, I.; Papkovsky, D. B. Imaging Oxygen in Neural Cell and Tissue Models by Means of Anionic Cell-Permeable Phosphorescent Nanoparticles. *Cell. Mol. Life Sci.* **2015**, *72* (2), 367−381.
(62) Dmitriev, R. I.; Borisov, S. M.; Jenkins, J.; Papkovsky, D. B. Multi-Parametric Imaging of Tumor Spheroids with Ultra-Bright and Tunable Nanoparticle O_2 Probes. In *Progress in Biomedical Optics and Imaging - Proceedings of SPIE*; SPIE, 2015; Vol. *9328*.
(63) Okkelman, I. A.; Vercruysse, C.; Kondrashina, A. V.; Borisov, S. M.; Dmitriev, R. I. Affordable Oxygen Microscopy-Assisted Biofabrication of Multicellular Spheroids. *J. Visualized Exp.* **2022**, *182*, No. e63403.
(64) Tsytsarev, V.; Arakawa, H.; Borisov, S.; Pumbo, E.; Erzurumlu, R. S.; Papkovsky, D. B. In Vivo Imaging of Brain Metabolism Activity Using a Phosphorescent Oxygen-Sensitive Probe. *J. Neurosci. Methods* **2013**, *216* (2), 146−151.
(65) Barra, J., Crosbourne, I., Wang, L., Bossardi-Ramos, R., Jourd'heuil, F., Nelson, I., Adam, A. P., Corr, D. T., Jourd'heuil, D., Barroso, M. DMT1 Bridges Endosomes and Mitochondria to Modulate Mitochondrial Iron Translocation. **2022**, bioRxiv, 488402.
(66) Ni, Y.; Wu, J. Far-Red and near Infrared BODIPY Dyes: Synthesis and Applications for Fluorescent PH Probes and Bio-Imaging. *Org. Biomol. Chem.* **2014**, *12* (23), 3774−3791.
(67) Tantama, M.; Hung, Y. P.; Yellen, G. Imaging Intracellular PH in Live Cells with a Genetically Encoded Red Fluorescent Protein Sensor. *J. Am. Chem. Soc.* **2011**, *133* (26), 10034−10037.
(68) Wu, J.; Abdelfattah, A. S.; Miraucourt, L. S.; Kutsarova, E.; Ruangkittisakul, A.; Zhou, H.; Ballanyi, K.; Wicks, G.; Drobizhev, M.; Rebane, A.; Ruthazer, E. S.; Campbell, R. E. A Long Stokes Shift Red Fluorescent Ca^{2+} Indicator Protein for Two-Photon and Ratiometric Imaging. *Nat. Commun.* **2014**, *5* (1), 5262.
(69) Feng, Y.; Cheng, J.; Zhou, L.; Zhou, X.; Xiang, H. Ratiometric Optical Oxygen Sensing: A Review in Respect of Material Design. *Analyst* **2012**, *137* (21), 4885−4901.
(70) Roussakis, E.; Ortines, R. V.; Pinsker, B. L.; Mooers, C. T.; Evans, C. L.; Miller, L. S.; Calderón-Colón, X. Theranostic Biocomposite Scaffold Membrane. *Biomaterials* **2019**, *212*, 17−27.
(71) Borisov, S. M.; Mayr, T.; Mistlberger, G.; Waich, K.; Koren, K.; Chojnacki, P.; Klimant, I. Precipitation as a Simple and Versatile Method for Preparation of Optical Nanochemosensors. *Talanta* **2009**, *79* (5), 1322−1330.
(72) Borisov, S. M.; Nuss, G.; Haas, W.; Saf, R.; Schmuck, M.; Klimant, I. New NIR-Emitting Complexes of Platinum(II) and Palladium(II) with Fluorinated Benzoporphyrins. *J. Photochem. Photobiol., A* **2009**, *201* (2−3), 128−135.
(73) Killoran, J.; Allen, L.; Gallagher, J. F.; Gallagher, W. M.; O'Shea, D. F. Synthesis of BF_2chelates of tetraarylazadipyrromethenes and evidence for their photodynamic therapeutic behaviour. *Chem. Commun.* **2002**, *8*, 1862−1863.
(74) Gorman, A.; Killoran, J.; O'Shea, C.; Kenna, T.; Gallagher, W.; O'Shea, D. In Vitro Demonstration of the Heavy-Atom Effect for Photodynamic Therapy. *J. Am. Chem. Soc.* **2004**, *126*, 10619−10631.
(75) Dmitriev, R. I.; Papkovsky, D. B. Intracellular Probes for Imaging Oxygen Concentration: How Good Are They? *Methods Appl. Fluoresc.* **2015**, *3* (3), 034001.
(76) Casey, R. C.; Burleson, K. M.; Skubitz, K. M.; Pambuccian, S. E.; Oegema, T. R.; Ruff, L. E.; Skubitz, A. P. N. β1-Integrins Regulate the Formation and Adhesion of Ovarian Carcinoma Multicellular Spheroids. *Am. J. Pathol.* **2001**, *159* (6), 2071−2080.
(77) Guillaume, O.; Kopinski-Grünwald, O.; Weisgrab, G.; Baumgartner, T.; Arslan, A.; Whitmore, K.; Van Vlierberghe, S.; Ovsianikov, A. Hybrid Spheroid Microscaffolds as Modular Tissue Units to Build Macro-Tissue Assemblies for Tissue Engineering. *Acta Biomater.* **2023**, *165*, 72−85.
(78) Kingsley, D. M.; Roberge, C. L.; Rudkouskaya, A.; Faulkner, D. E.; Barroso, M.; Intes, X.; Corr, D. T. Laser-Based 3D Bioprinting for Spatial and Size Control of Tumor Spheroids and Embryoid Bodies. *Acta Biomater.* **2019**, *95*, 357−370.
(79) Peirsman, A.; Blondeel, E.; Ahmed, T.; Anckaert, J.; Audenaert, D.; Boterberg, T.; Buzas, K.; Carragher, N.; Castellani, G.; Castro, F.; Dangles-Marie, V.; Dawson, J.; De Tullio, P.; De Vlieghere, E.;

https://doi.org/10.1021/acsnano.3c12539
ACS Nano 2024, 18, 12168−12186

Dedeyne, S.; Depypere, H.; Diosdi, A.; Dmitriev, R. I.; Dolznig, H.; Fischer, S.; Gespach, C.; Goossens, V.; Heino, J.; Hendrix, A.; Horvath, P.; Kunz-Schughart, L. A.; Maes, S.; Mangodt, C.; Mestdagh, P.; Michlíková, S.; Oliveira, M. J.; Pampaloni, F.; Piccinini, F.; Pinheiro, C.; Rahn, J.; Robbins, S. M.; Siljamäki, E.; Steigemann, P.; Sys, G.; Takayama, S.; Tesei, A.; Tulkens, J.; Van Waeyenberge, M.; Vandesompele, J.; Wagemans, G.; Weindorfer, C.; Yigit, N.; Zablowsky, N.; Zanoni, M.; Blondeel, P.; De Wever, O. MISpheroID: a knowledgebase and transparency tool for minimum information in spheroid identity. *Nat. Methods* **2021**, *18* (11), 1294−1303.

(80) Vande Voorde, J.; Ackermann, T.; Pfetzer, N.; Sumpton, D.; Mackay, G.; Kalna, G.; Nixon, C.; Blyth, K.; Gottlieb, E.; Tardito, S. Improving the Metabolic Fidelity of Cancer Models with a Physiological Cell Culture Medium. *Sci. Adv.* **2019**, *5* (1), No. eaau7314.

(81) Lagziel, S.; Gottlieb, E.; Shlomi, T. Mind Your Media. *Nat. Metab.* **2020**, *2* (12), 1369−1372.

(82) Froehlich, K.; Haeger, J.-D.; Heger, J.; Pastuschek, J.; Photini, S. M.; Yan, Y.; Lupp, A.; Pfarrer, C.; Mrowka, R.; Schleußner, E.; Markert, U. R.; Schmidt, A. Generation of Multicellular Breast Cancer Tumor Spheroids: Comparison of Different Protocols. *J. Mammary Gland Biol. Neoplasia* **2016**, *21* (3−4), 89−98.

(83) Pittman, M.; Iu, E.; Li, K.; Wang, M.; Chen, J.; Taneja, N.; Jo, M. H.; Park, S.; Jung, W.-H.; Liang, L.; Barman, I.; Ha, T.; Gaitanaros, S.; Liu, J.; Burnette, D.; Plotnikov, S.; Chen, Y. Membrane Ruffling Is a Mechanosensor of Extracellular Fluid Viscosity. *Nat. Phys.* **2022**, *18*, 1112−1121.

(84) Bera, K.; Kiepas, A.; Godet, I.; Li, Y.; Mehta, P.; Ifemembi, B.; Paul, C. D.; Sen, A.; Serra, S. A.; Stoletov, K.; Tao, J.; Shatkin, G.; Lee, S. J.; Zhang, Y.; Boen, A.; Mistriotis, P.; Gilkes, D. M.; Lewis, J. D.; Fan, C.-M.; Feinberg, A. P.; Valverde, M. A.; Sun, S. X.; Konstantopoulos, K. Extracellular Fluid Viscosity Enhances Cell Migration and Cancer Dissemination. *Nature* **2022**, *611* (7935), 365−373.

(85) Novotný, J.; Strnadová, K.; Dvořánková, B.; Kocourková, Š.; Jakša, R.; Dundr, P.; Paces, V.; Smetana, K.; Kolar, M.; Lacina, L. Single-Cell RNA Sequencing Unravels Heterogeneity of the Stromal Niche in Cutaneous Melanoma Heterogeneous Spheroids. *Cancers* **2020**, *12*, 3324.

(86) Han, S. J.; Kwon, S.; Kim, K. S. Challenges of Applying Multicellular Tumor Spheroids in Preclinical Phase. *Cancer Cell Int.* **2021**, *21* (1), 152.

(87) Muciño-Olmos, E. A.; Vázquez-Jiménez, A.; Avila-Ponce de León, U.; Matadamas-Guzman, M.; Maldonado, V.; López-Santaella, T.; Hernández-Hernández, A.; Resendis-Antonio, O. Unveiling Functional Heterogeneity in Breast Cancer Multicellular Tumor Spheroids through Single-Cell RNA-Seq. *Sci. Rep.* **2020**, *10* (1), 12728.

(88) Rankin, E. B.; Giaccia, A. J. Hypoxic Control of Metastasis. *Science* **2016**, *352* (6282), 175−180.

(89) Okkelman, I. A.; Neto, N.; Papkovsky, D. B.; Monaghan, M. G.; Dmitriev, R. I. A Deeper Understanding of Intestinal Organoid Metabolism Revealed by Combining Fluorescence Lifetime Imaging Microscopy (FLIM) and Extracellular Flux Analyses. *Redox Biol.* **2020**, *30*, 101420.

(90) Baye, J.; Galvin, C.; Shen, A. Microfluidic Device Flow Field Characterization around Tumor Spheroids with Tunable Necrosis Produced in an Optimized Off-Chip Process. *Biomed. Microdevices* **2017**, *19*, 59.

(91) Raghavan, S.; Mehta, P.; Horst, E. N.; Ward, M. R.; Rowley, K. R.; Mehta, G. Comparative Analysis of Tumor Spheroid Generation Techniques for Differential in Vitro Drug Toxicity. *Oncotarget* **2016**, *7*, 16948−16961.

(92) Al-Ani, A.; Toms, D.; Kondro, D.; Thundathil, J.; Yu, Y.; Ungrin, M. Oxygenation in Cell Culture: Critical Parameters for Reproducibility Are Routinely Not Reported. *PLoS One* **2018**, *13* (10), No. e0204269.

(93) Somerville, G. A.; Proctor, R. A. Cultivation Conditions and the Diffusion of Oxygen into Culture Media: The Rationale for the Flask-to-Medium Ratio in Microbiology. *BMC Microbiol.* **2013**, *13* (1), 9.

(94) Mueller-Klieser, W.; Freyer, J.; Sutherland, R. M. Influence of Glucose and Oxygen Supply Conditions on the Oxygenation of Multicellular Spheroids. *Br. J. Cancer* **1986**, *53*, 345−353.

(95) Talari, A. C. S.; Raza, A.; Rehman, S.; Rehman, I. U. Analysing Normal Proliferating, Hypoxic and Necrotic Regions of T-47D Human Breast Cancer Spheroids Using Raman Spectroscopy. *Appl. Spectrosc. Rev.* **2017**, *52*, 909.

(96) Blacker, T. S.; Duchen, M. R. Investigating Mitochondrial Redox State Using NADH and NADPH Autofluorescence. *Free Radicals Biol. Med.* **2016**, *100*, 53−65.

(97) Barroso, M.; Monaghan, M. G.; Niesner, R.; Dmitriev, R. I. Probing Organoid Metabolism Using Fluorescence Lifetime Imaging Microscopy (FLIM): The next Frontier of Drug Discovery and Disease Understanding. *Adv. Drug Delivery Rev.* **2023**, *201*, 115081.

(98) Matoba, S.; Kang, J.-G.; Patino, W. D.; Wragg, A.; Boehm, M.; Gavrilova, O.; Hurley, P. J.; Bunz, F.; Hwang, P. M. P53 Regulates Mitochondrial Respiration. *Science* **2006**, *312* (5780), 1650−1653.

(99) Datta, R.; Heaster, T.; Sharick, J.; Gillette, A.; Skala, M. Fluorescence Lifetime Imaging Microscopy: Fundamentals and Advances in Instrumentation, Analysis, and Applications. *J. Biomed. Opt.* **2020**, *25*, 1.

(100) Karrobi, K.; Tank, A.; Fuzail, M. A.; Kalidoss, M.; Tilbury, K.; Zaman, M.; Ferruzzi, J.; Roblyer, D. Fluorescence Lifetime Imaging Microscopy (FLIM) Reveals Spatial-Metabolic Changes in 3D Breast Cancer Spheroids. *Sci. Rep.* **2023**, *13* (1), 3624.

(101) Alfonso-Garcia, A.; Bec, J.; Weyers, B.; Marsden, M.; Zhou, X.; Li, C.; Marcu, L. Mesoscopic Fluorescence Lifetime Imaging: Fundamental Principles, Clinical Applications and Future Directions. *J. Biophotonics* **2021**, *14* (6), No. e202000472.

(102) Peng, X.; Huang, J.; Li, M.; Chen, Z.; Yan, W.; Qu, J. Lipid Membrane Alterations in Tumor Spheroids Revealed by Fluorescence Lifetime Microscopy Imaging. *Anal. Chem.* **2022**, *95* (2), 575−580.

(103) Ouyang, Y.; Liu, Y.; Wang, Z. M.; Liu, Z.; Wu, M. FLIM as a Promising Tool for Cancer Diagnosis and Treatment Monitoring. *Nanomicro Lett.* **2021**, *13* (1), 133.

(104) Dmitriev, R. I.; Intes, X.; Barroso, M. M. Luminescence Lifetime Imaging of Three-Dimensional Biological Objects. *J. Cell Sci.* **2021**, *134* (9), 1−17.

(105) Shirmanova, M. V.; Druzhkova, I. N.; Lukina, M. M.; Matlashov, M. E.; Belousov, V. V.; Snopova, L. B.; Prodanetz, N. N.; Dudenkova, V. V.; Lukyanov, S. A.; Zagaynova, E. V. Intracellular PH Imaging in Cancer Cells in Vitro and Tumors in Vivo Using the New Genetically Encoded Sensor SypHer2. *Biochim. Biophys. Acta, Gen. Subj.* **2015**, *1850* (9), 1905−1911.

(106) Roussakis, E.; Ortines, R. V.; Pinsker, B. L.; Mooers, C. T.; Evans, C. L.; Miller, L. S.; Calderón-Colón, X. Theranostic Biocomposite Scaffold Membrane. *Biomaterials* **2019**, *212*, 17−27.

(107) Bose, S.; Barroso, M.; Chheda, M. G.; Clevers, H.; Elez, E.; Kaochar, S.; Kopetz, S. E.; Li, X.-N.; Meric-Bernstam, F.; Meyer, C. A.; Mou, H.; Naegle, K. M.; Pera, M. F.; Perova, Z.; Politi, K. A.; Raphael, B. J.; Robson, P.; Sears, R. C.; Tabernero, J.; Tuveson, D. A.; et al. A Path to Translation: How 3D Patient Tumor Avatars Enable next Generation Precision Oncology. *Cancer Cell* **2022**, *40*, 1448−1453.

(108) Pasch, C. A.; Favreau, P. F.; Yueh, A. E.; Babiarz, C. P.; Gillette, A. A.; Sharick, J. T.; Karim, M. R.; Nickel, K. P.; DeZeeuw, A. K.; Sprackling, C. M.; Emmerich, P. B.; DeStefanis, R. A.; Pitera, R. T.; Payne, S. N.; Korkos, D. P.; Clipson, L.; Walsh, C. M.; Miller, D.; Carchman, E. H.; Burkard, M. E.; Lemmon, K. K.; Matkowskyj, K. A.; Newton, M. A.; Ong, I. M.; Bassetti, M. F.; Kimple, R. J.; Skala, M. C.; Deming, D. A. Patient-Derived Cancer Organoid Cultures to Predict Sensitivity to Chemotherapy and Radiation. *Clin. Cancer Res.* **2019**, *25* (17), 5376−5387.

(109) Debruyne, A. C.; Okkelman, I. A.; Dmitriev, R. I. Balance between the Cell Viability and Death in 3D. *Semin. Cell Dev. Biol.* **2023**, *144*, 55−66.

https://doi.org/10.1021/acsnano.3c12539
ACS Nano 2024, 18, 12168−12186

(110) Banerjee, D.; Singh, Y. P.; Datta, P.; Ozbolat, V.; O'Donnell, A.; Yeo, M.; Ozbolat, I. T. Strategies for 3D Bioprinting of Spheroids: A Comprehensive Review. *Biomaterials* **2022**, *291*, 121881.
(111) Hutter, L. H.; Müller, B. J.; Koren, K.; Borisov, S. M.; Klimant, I. Robust Optical Oxygen Sensors Based on Polymer-Bound NIR-Emitting Platinum(Ii)−Benzoporphyrins. *J. Mater. Chem. C* **2014**, *2* (36), 7589−7598.
(112) Dmitriev, R. I.; Papkovsky, D. B. In Vitro Ischemia Decreases Histone H4K16 Acetylation in Neural Cells. *FEBS Lett.* **2015**, *589* (1), 138−144.
(113) Fomin, M. A.; Dmitriev, R. I.; Jenkins, J.; Papkovsky, D. B.; Heindl, D.; König, B. Two-Acceptor Cyanine-Based Fluorescent Indicator for NAD(P)H in Tumor Cell Models. *ACS Sens.* **2016**, *1* (6), 702−709.
(114) Gonzalez-Castillo, C.; Rubio, R.; Zenteno-Savin, T. Coronary Flow-Induced Inotropism Is Modulated by Binding of Dextrans to the Endothelial Luminal Surface. *Am. J. Physiol.: Heart Circ. Physiol.* **2003**, *284*, H1348−H1357.
(115) Russegger, A.; Debruyne, A. C.; Berrio, D. C.; Fuchs, S.; Marzi, J.; Schenke-Layland, K.; Dmitriev, R. I.; Borisov, S. M. Bright and Photostable TADF-Emitting Zirconium(IV) Pyridinedipyrrolide Complexes: Efficient Dyes for Decay Time-Based Temperature Sensing and Imaging. *Adv. Opt. Mater.* **2023**, *11* (9), 2202720.
(116) Leben, R.; Köhler, M.; Radbruch, H.; Hauser, A. E.; Niesner, R. A. Systematic Enzyme Mapping of Cellular Metabolism by Phasor-Analyzed Label-Free NAD(P)H Fluorescence Lifetime Imaging. *Int. J. Mol. Sci.* **2019**, *20*, 5565.
(117) Schroeder, A. B.; Dobson, E. T. A.; Rueden, C. T.; Tomancak, P.; Jug, F.; Eliceiri, K. W. The ImageJ. Ecosystem: Open-Source Software for Image Visualization, Processing, and Analysis. *Protein Sci.* **2021**, *30* (1), 234−249.

https://doi.org/10.1021/acsnano.3c12539
ACS Nano 2024, 18, 12168−12186